This article was downloaded by:
On: *21 January 2011*
Access details: *Access Details: Free Access*
Publisher *Taylor & Francis*
Informa Ltd Registered in England and Wales Registered Number: 1072954 Registered office: Mortimer House, 37-41 Mortimer Street, London W1T 3JH, UK

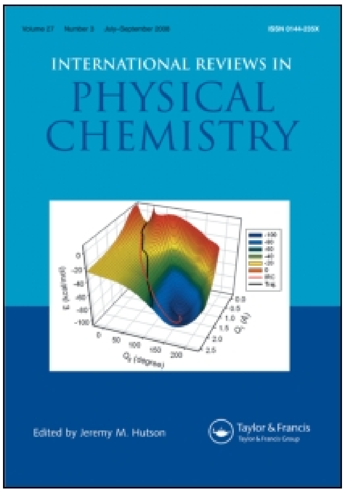

International Reviews in Physical Chemistry
Publication details, including instructions for authors and subscription information:
http://www.informaworld.com/smpp/title~content=t713724383

Using the MCTDH wavepacket propagation method to describe multimode non-adiabatic dynamics

G. A. Worth[a]; H. -D. Meyer[b]; H. Köppel[b]; L. S. Cederbaum[b]; I. Burghardt[c]
[a] School of Chemistry, University of Birmingham, B15 2TT, UK [b] Theoretische Chemie, Heidelberg Universität, D-69120 Heidelberg, Germany [c] Département de Chimie, Ecole Normale Supérieure, Paris cedex 05, France

To cite this Article Worth, G. A. , Meyer, H. -D. , Köppel, H. , Cederbaum, L. S. and Burghardt, I.(2008) 'Using the MCTDH wavepacket propagation method to describe multimode non-adiabatic dynamics', International Reviews in Physical Chemistry, 27: 3, 569 — 606

To link to this Article: DOI: 10.1080/01442350802137656

URL: http://dx.doi.org/10.1080/01442350802137656

PLEASE SCROLL DOWN FOR ARTICLE

Full terms and conditions of use: http://www.informaworld.com/terms-and-conditions-of-access.pdf

This article may be used for research, teaching and private study purposes. Any substantial or systematic reproduction, re-distribution, re-selling, loan or sub-licensing, systematic supply or distribution in any form to anyone is expressly forbidden.

The publisher does not give any warranty express or implied or make any representation that the contents will be complete or accurate or up to date. The accuracy of any instructions, formulae and drug doses should be independently verified with primary sources. The publisher shall not be liable for any loss, actions, claims, proceedings, demand or costs or damages whatsoever or howsoever caused arising directly or indirectly in connection with or arising out of the use of this material.

International Reviews in Physical Chemistry
Vol. 27, No. 3, July–September 2008, 569–606

Taylor & Francis
Taylor & Francis Group

RESEARCH ARTICLE

Using the MCTDH wavepacket propagation method to describe multimode non-adiabatic dynamics

G. A. Worth[a]*, H.-D. Meyer[b], H. Köppel[b], L. S. Cederbaum[b] and I. Burghardt[c]

[a]*School of Chemistry, University of Birmingham, Birmingham, B15 2TT, UK;* [b]*Theoretische Chemie, Heidelberg Universität, Im Neuenheimer Feld 229, D-69120 Heidelberg, Germany;* [c]*Département de Chimie, Ecole Normale Supérieure, 24 rue Lhomond, Paris cedex 05, France*

(*Received 14 March 2008; final version received 17 April 2008*)

The MCTDH method has been used successfully to treat the non-adiabatic dynamics of a number of systems. These are hard problems due to the number of modes that need to be included in a calculation, and the strong coupling between the nuclear and electronic motion at conical intersections connecting electronic states in these systems. In this review, an overview of the basic theory of the method is given highlighting how it is able to treat larger systems than other quantum dynamics methods. The vibronic coupling model Hamiltonian is also described, which provides a good starting point for the description of these systems. Examples of calculations made and systems treated are given. Finally, a development of the basic MCTDH method in which some of the usual time-dependent basis functions are replaced by Gaussian wavepackets is outlined. This method promises not only to treat larger systems, but to provide a consistent quantum–semiclassical framework.

Keywords: quantum dynamics simulations; the MCTDH method; non-adiabatic population transfer; conical intersections; theoretical chemistry

Contents

PAGE
1. **Introduction** 570
2. **MCTDH theory** 572
    2.1. Wavefunction ansatz and equations of motion 572
    2.2. Efficiency and memory requirements 574
    2.3. Multi-state calculations 577
3. **Photo-absorption spectra** 578
4. **State populations** 580
5. **The vibronic coupling Hamiltonian** 581
6. **Combining the vibronic coupling model with MCTDH** 584

---

*Corresponding author. Email: G.A.Worth@bham.ac.uk

ISSN 0144–235X print/ISSN 1366–591X online
© 2008 Taylor & Francis
DOI: 10.1080/01442350802137656
http://www.informaworld.com

7. Examples 587
7.1. Allene cation 587
7.2. $Cr(CO)_5$ 589
7.3. Benzene cation 591

8. Parameterized basis functions: G-MCTDH 593

9. Summary and conclusions 601

Acknowledgements 603

References 603

1. Introduction

Quantum dynamics simulations have become increasingly important to provide a detailed description of a phenomenon in terms of the underlying molecular nature of the system. Solving the time-dependent Schrödinger equation variationally using a straightforward basis-set expansion of the wavefunction is known simply as *wavepacket dynamics*. Wavepacket propagation methods are particularly attractive: they are simple to implement, and provide easily visualizable results of the evolving system that can be easily related to experiment. The most powerful wavepacket dynamics algorithm at present, able to treat larger systems than the standard method, is multi-configurational time-dependent Hartree (MCTDH). The algorithm is, however not simple to use.

The MCTDH algorithm was introduced in 1990 by Meyer, Manthe, and Cederbaum [1]. A first comprehensive description of the method – together with the first non-trivial application (photo-dissociation of NOCl) – appeared two years later [2]. The basic theory of MCTDH has been discussed in great detail in two review articles [3,4] and in a forthcoming book [5], from which parts of this review are taken. Hence in the following only an overview of MCTDH theory is given, highlighting the features that give the method its power and flexibility.

A class of problems that have been treated with particular success by the MCTDH method are those in which a conical intersection between potential energy surfaces dominates the dynamics. These non-adiabatic systems – so called as they cannot be described by a single adiabatic potential energy surface – are able to undergo radiationless electronic state crossing on an ultrafast (femtosecond) time-scale [6,7]. In fact one of first applications of MCTDH was to the non-adiabatic photo-dissociation of CH_3I [8,9] – a five dimensional calculation which even now is beyond the capabilities of most quantum dynamics methods.

The signature of conical intersections are found in many spectra, particularly photo-electron spectra [10–12], and they provide important pathways in photo-chemistry [13,14] in systems ranging from H_3 [15,16] to biologically active chromophores such as retinal [17,18] and DNA bases [19,20]. Non-adiabatic effects are also important in electron transfer problems [21,22].

Wavepacket dynamics simulations have a natural connection to detailed experiments using femtochemistry laser spectroscopy, and simulations are routinely required to aid the interpretation of these studies. The main hurdles for simulations are due to the size of the systems studied. Non-adiabatic phenomena are inherently multi-dimensional in nature, often with a number of vibrational modes coupled strongly to the electronic degree of freedom. A typical example is provided by the absorption spectrum of pyrazine ($C_4N_2H_4$). The conical intersection connecting the S_1 and S_2 states strongly couples five vibrational modes to the electronic motion, and weakly couples the remaining 19 [23]. Not only is such a system too large to simulate using standard wavepacket dynamics methods, but there is also the problem of obtaining suitable potential energy surfaces.

A powerful, yet simple description of coupled potential surfaces is provided by the vibronic-coupling model Hamiltonian which uses the correspondence between the adiabatic and diabatic pictures to full effect [12]. The adiabatic picture is that provided by the clamped-nucleus Hamiltonian, with sets of energy-ordered potential energy surfaces provided by the electronic states. Coupling between these states is provided by nuclear momentum-like operators. The diabatic picture is one in which a potential energy surface is related to an electronic configuration, and so can be related to chemical entities. Couplings are provided by potential-like operators. The surfaces in the diabatic picture, as they are smooth, can be described by a low-order Taylor expansion. Electronic structure calculations, however, lead to the well-defined adiabatic surfaces.

The vibronic-coupling model, described in Section 5, thus provides a Hamiltonian for treating non-adiabatic phenomena. In addition to its simplicity, it is in the product-form which allows the efficient application of the MCTDH algorithm (Section 2.2). In Section 6 an example is used to show how the MCTDH method is able to treat large problems using the model Hamiltonian: a 10-mode two-state system is straightforward, a 24-mode two-state system is possible. After that in Section 7 examples are given of problems that have been treated.

As the full wavefunction is obtained, it can be analysed to obtain a range of information. The simplest are state populations and coordinate expectation values that describe the system evolution. Spectra in the Condon approximation can also be obtained from the autocorrelation function (Section 3). More complicated analyses are also possible if a laser pulse is included explicitely into a calculation. These, a straightforward addition in MCTDH [24], allow optimal control calculations, in which a laser field can be designed to control the system evolution [25]. Alternatively, a time-resolved spectrum, such as a time-resolved photo-electron spectrum, can be calculated [26].

An exciting development at present is the use of parametrized basis functions in the MCTDH method. This, the G-MCTDH method, was introduced by Burghardt *et al.* in 1999 [27]. By using Gaussian basis functions to describe some, or all, modes it is possible to provide better scaling and promises access to even larger systems than those accessible to the standard MCTDH method. Connections to semi-classical and mixed quantum-classical methods are also made. This is described in Section 8.

The Gaussian functions of the G-MCTDH method provide localized basis functions. The algorithm thus provides the framework for *direct dynamics* calculations, in which the potential energy surfaces are calculated on-the-fly using quantum chemistry programs as and when they are needed. This is an attractive idea. By removing the need to calculate the potential surfaces before a system can be studied, it opens up the possibility of doing quantum dynamics calculations as simply as quantum chemistry calculations. They also promise to be efficient for large systems, as only the relevant region of configuration space is searched. Such calculations are not further treated in this article, but are dealt with in a recent review [28].

2. MCTDH theory

2.1. *Wavefunction ansatz and equations of motion*

The basis of the MCTDH method is the use of the following wavefunction ansatz to solve the time-dependent Schrödinger equation for a physical system with f degrees of freedom (DOFs) described by coordinates $q_1, \ldots, q_f$:

$$\begin{aligned}\Psi(q_1, \ldots q_f, t) &= \sum_{j_1=1}^{n_1} \cdots \sum_{j_p=1}^{n_p} A_{j_1 \ldots j_p}(t) \varphi_{j_1}^{(1)}(Q_1, t) \ldots \varphi_{j_p}^{(p)}(Q_p, t) \\ &= \sum_J A_J \Phi_J. \end{aligned} \tag{1}$$

Equation (1) is a direct product expansion of p sets of orthonormal time-dependent basis functions $\{\varphi^{(\kappa)}\}$, known as *single-particle functions* (SPFs). The coordinate for each set of n_κ functions is a composite coordinate of one or more system coordinates

$$Q_\kappa = (q_a, q_b, \ldots). \tag{2}$$

Thus the basis functions are d-dimensional, where d is the number of system coordinates that have been combined together and treated as one "particle". (Typically $d = 1$–4.) The second line in Equation (1), defines the composite index $J = j_1 \ldots j_p$ and the *Hartree product* Φ_J. The ansatz looks similar to the standard wavepacket expansion [29–31], except that the SPFs provide a time-dependent basis set.

Using this ansatz, a variational solution to the time-dependent Schrödinger equation is provided by a coupled set of equations, one for the expansion coefficients:

$$i\dot{\mathbf{A}} = \boldsymbol{\mathcal{K}}\mathbf{A}, \tag{3}$$

and one for each set of SPFs

$$i\dot{\boldsymbol{\varphi}}^{(\kappa)} = \left(1 - P^{(\kappa)}\right)\left(\boldsymbol{\rho}^{(\kappa)}\right)^{-1} \boldsymbol{\mathcal{H}}^{(\kappa)} \boldsymbol{\varphi}^{(\kappa)}. \tag{4}$$

A matrix notation has been used with the A-coefficients and SPFs written as vectors, i.e. $\boldsymbol{\varphi}^{(\kappa)} = (\varphi_1^{(\kappa)}, \ldots, \varphi_{n_\kappa}^{(\kappa)})^T$.

The matrix $\boldsymbol{\mathcal{K}}$ is the Hamiltonian operator represented in the basis of Hartree products

$$\mathcal{K}_{JL} = \langle \Phi_J \mid H \mid \Phi_L \rangle. \tag{5}$$

Thus Equation (3) has the same form as the equations of motion for standard wavepacket propagation. The difference is that the Hamiltonian matrix is time-dependent due to the time-dependence of the SPFs.

The equations of motion for the SPFs contain three new entities. The first is the projector onto the space spanned by the SPFs

$$P^{(\kappa)} = \sum_j \left|\varphi_j^{(\kappa)}\right\rangle \left\langle \varphi_j^{(\kappa)}\right|. \tag{6}$$

The operator $(1 - P^{(\kappa)})$ ensures that the time-derivative of the SPFs is orthogonal to the space spanned by the functions. Thus any changes cover new regions. When the basis set is complete, the SPFs become time-independent and the equations of motion are identical to the standard method. If the SPFs do not provide a complete basis set, then they move so as to provide the best possible basis for the description of the evolving wavepacket. This optimal description is ensured by the variational method used for the derivation.

For the other two new entities it is useful to introduce the *single-hole functions*, $\Psi_a^{(\kappa)}$, which is the wavefunction associated with the *j*-th SPF of the κ-th particle. As the total wavefunction lies in the space spanned by the SPFs one can make use of the completeness relation and write

$$\Psi = \sum_a \left|\varphi_a^{(\kappa)}\right\rangle \left\langle\varphi_a^{(\kappa)}\middle|\Psi\right\rangle = \sum_a \varphi_a^{(\kappa)}\, \Psi_a^{(\kappa)}. \tag{7}$$

To make this clear, the single-hole function for the first particle is

$$\Psi_a^{(1)} = \sum_{j_2=1}^{n_1} \cdots \sum_{j_p=1}^{n_p} A_{aj_2\ldots j_p} \varphi_{j_2}^{(2)} \ldots \varphi_{j_p}^{(p)}. \tag{8}$$

The *single-hole index*, J_a^κ, is also useful to keep the notation compact. The index can take any values except for the κ-th position which has a value a. Thus, there is the single-hole coefficient $A_{J_a^\kappa}$ and single-hole Hartree product Φ_{J^κ} which allow the single-hole function to be written

$$\Psi_a^{(\kappa)} = \sum_{J^\kappa} A_{J_a^\kappa}\, \Phi_{J^\kappa}, \tag{9}$$

where $\sum_{J^\kappa}$ is the sum over all index values keeping the value of the κ-th index fixed; J^κ is a composite index similar to J but with the κ-th entry removed.

Using this new notation, the *mean-field operator matrix*, $\mathcal{H}^{(\kappa)}$ can be easily written as

$$\mathcal{H}_{ab}^{(\kappa)} = \left\langle\Psi_a^{(\kappa)}\middle| H \middle|\Psi_b^{(\kappa)}\right\rangle. \tag{10}$$

The integration in the brackets is over all particles except κ. This operator on the κ-th particle correlates the motion between the different sets of SPFs.

Finally, the *density matrix* $\rho^{(\kappa)}$ is

$$\begin{aligned} \rho_{ab}^{(\kappa)} &= \left\langle\Psi_a^{(\kappa)}\middle|\Psi_b^{(\kappa)}\right\rangle \\ &= \sum_{J^\kappa} A_{J_a^\kappa}^* A_{J_b^\kappa}. \end{aligned} \tag{11}$$

The density matrices, which enter the equations of motion for the SPFs, Equation (4), as its inverse, can be used to provide a useful measure of the quality of the calculation. In an analogous way to the use of density matrices in electronic structure theory, the eigenfunctions of this matrix are termed *natural orbitals* and the eigenvalues provide populations for these functions. The lower the population, the less important the function. As the space spanned by the natural orbitals is equivalent to that of the original SPFs, if the population of the highest natural orbital is such that the function is effectively not required for an accurate description of the evolving wavepacket, the MCTDH wavefunction is of a good quality. As a rule of thumb averaged quantities such as expectation values and spectra are converged when the highest natural orbitals have a population less than 10^{-3}. Other quantities such as cross-sections are more sensitive to errors in the wavefunction and the populations have to drop below 10^{-6} for converged results.

2.2. *Efficiency and memory requirements*

Standard wavepacket dynamics uses a wavefunction ansatz like that of Equation (1), except with a set of time-independent basis functions for each DOF rather than a set of time-dependent functions for each particle. While the number of basis functions may vary for each DOF, if N is representative of this number, then the wavefunction is represented by N^f expansion coefficients. This is the basis of the exponential increase of computer resources with system size that plagues wavepacket dynamics. As $N \sim 50$ is reasonable, a four-dimensional system using double-precision complex arithmetic requires nearly 100 MB of memory just to store one wavefunction, while a five-dimensional system requires of the order of 4.8 GB. Clearly this scaling severely limits the size of system treatable by these methods.

In comparison, the MCTDH wavefunction requires

$$\text{memory} \sim n^p + pnN^d \tag{12}$$

where n is characteristic of the number of SPFs for the p particles. The first term is the number of A-coefficients. The second term is due to the representation of the SPFs through *primitive basis functions*

$$\varphi_j^{(\kappa)}(Q_\kappa) = \sum_{k=1}^{N_\kappa} a_{kj}^{(\kappa)} \chi_k^{(\kappa)}(Q_\kappa). \tag{13}$$

Typically, a *discrete variable representation* (DVR) is used for this. DVRs are the time-independent bases used in standard wavepacket propagation calculations. A number of different DVRs have been developed, suitable for use for different types of coordinates. Examples are the harmonic oscillator DVR used for vibrational motion, Legendre DVR for rotations, and exponential and sine DVRs used for free motion with or without periodic boundary conditions. A related method is to use a collocation grid and FFT methods to evaluate the kinetic energy operator. An overview of the properties of different DVRs and FFT methods is given in Appendix B of [3].

There are two limits to be examined. The first is when $p = f$ and $d = 1$, i.e. all particles are one-dimensional. Here the first term dominates. Using reasonable values of $N = 50$ and $n = 10$ then for $f = 4$ the MCTDH wavefunction requires a tiny 0.18 MB and for $f = 5$ still only 1.56 MB. This is obviously much less than the memory required to store the full primitive grid. The exponential wall still hits the method, however, and 153 GB is needed for each wavefunction if $f = 10$. The other limit to be studied is when all DOFs are combined together so that only one particle is present. Thus $p = 1$ and $d = f$. In this limit $n = 1$ and the first term in Equation (12) is always 1. The second term then dominates and of course is simply the size of the full primitive grid, N^f, as in this limit the MCTDH method is identical to the standard wavepacket method. A single wavefunction now takes 1.5×10^9 GB. In between these two limits there is a trade-off between the memory required by the A-coefficients and that required by the SPFs. Thus, if two-dimensional particles are used in a 10-dimensional calculation, $f=10$, $p=5$, $d=2$ and the memory required is 3.4 MB per wavefunction evenly distributed between the two parts.

The figures used above assume that $n=10$ is a suitable figure regardless of how many DOFs are combined together into each particle. This is of course not the case. Imagine n SPFs are required for each particle in a problem where $p=f$, i.e. all particles are one-dimensional. If a second calculation is then made using two-dimensional particles, i.e. $p=f/2$, then $\tilde{n}$, the number of SPFs required in the new calculation will be different from n, but $\tilde{n}<n^2$ ($\tilde{n}=dn$ is a reasonable rule of thumb). The upper limit is because correlations between these modes are now included at the SPF level. For large combinations, $\tilde{n}<n$ is possible as in the limit that all DOFs are combined together $\tilde{n}=1$: only a single SPF – the exact wavefunction – is required. When choosing which DOFs should be combined together it is thus useful to put strongly correlated modes in one particle as this significantly reduces the number of SPFs, and thus configurations, required. If the amount of correlation among the DOFs is not known, one should combine DOFs which are characterized by similar vibrational frequencies. One must be mindful, however, that the particle grid lengths do not get too long. For a balanced calculation particles should be chosen with similar grid lengths.

To solve the equations of motion for the A-coefficients and SPFs, Equations (3, 4), the elements of the Hamiltonian matrix, $\boldsymbol{\mathcal{K}}$ need to be evaluated:

$$\left\langle \varphi^{(1)}_{j_1}\dots\varphi^{(p)}_{j_p} \right| H \left| \varphi^{(1)}_{k_1}\dots\varphi^{(p)}_{k_p} \right\rangle = \left\langle \varphi^{(1)}_{j_1}\dots\varphi^{(p)}_{j_p} \right| T+V \left| \varphi^{(1)}_{k_1}\dots\varphi^{(p)}_{k_p} \right\rangle. \tag{14}$$

Elements of the mean-field matrices are also required, $\boldsymbol{\mathcal{H}}^{(\kappa)}$, and the techniques described below can be used for these too.

If the basis functions are DVRs this multi-dimensional integral would be straightforward. A set of DVR functions along a coordinate q_ν, $\{\chi^{(\nu)}(q_\nu)\}$ has the property that their matrix representation of the position operator, $\hat{q}_\nu$, is diagonal, i.e.

$$\left\langle \chi^{(\nu)}_i \right| q_\nu \left| \chi^{(\nu)}_j \right\rangle = q^{(\nu)}_j \delta_{ij}, \tag{15}$$

and the values q_ν provide a grid of points related to the DVR functions. As a result, if there are enough functions for the set to be effectively complete, the potential energy operator can be taken as diagonal in this basis

$$\left\langle \chi^{(1)}_{i_1}\dots\chi^{(f)}_{i_f} \right| V \left| \chi^{(1)}_{j_1}\dots\chi^{(f)}_{j_f} \right\rangle = V\left(q^{(1)}_{j_1},\dots,q^{(f)}_{j_f}\right)\delta_{i_1 j_1}\dots\delta_{i_f j_f} \tag{16}$$

and the integral is obtained by evaluating the potential energy only at the grid point $q^{(1)}_{j_1},\dots,q^{(f)}_{j_f}$.

The kinetic energy operator usually only acts on a single coordinate and matrix elements can be evaluated analytically in the related finite basis representation (FBR). The FBR-DVR transformation is then used to give $\{\phi^{(\nu)}\}$

$$\left\langle \chi^{(\nu)}_i \right| T_\nu \left| \chi^{(\nu)}_j \right\rangle = \sum_{kl} U^{(\nu)}_{ik} \left\langle \phi^{(\nu)}_i \right| T_\nu \left| \phi^{(\nu)}_j \right\rangle \left(U^{(\nu)}_{lj}\right)^\dagger. \tag{17}$$

Thus the potential energy is obtained by evaluating the potential function at N^f points, and the kinetic energy by transforming N^2 matrices. At no time is it necessary to evaluate multi-dimensional integrals, and the full N^{2f} Hamiltonian matrix does not need to be built.

In MCTDH the potential energy matrix elements can be obtained by transforming from the SPF basis to the DVR. Using Equation (13) and the DVR potential energy Equation (16), this is

$$\left\langle \varphi_{i_1}^{(1)} \dots \varphi_{i_p}^{(p)} \right| V \left| \varphi_{j_1}^{(1)} \dots \varphi_{j_p}^{(p)} \right\rangle = \sum_{i_1 \dots i_p} \sum_{j_1 \dots j_p} a_{k_1 i_1}^{(1)*} \dots a_{k_p i_1}^{(p)*} a_{k_1 j_1}^{(1)} \dots a_{k_p j_1}^{(p)} V\left(Q_{k_1}^{(1)}, \dots Q_{k_p}^{(p)} \right). \tag{18}$$

The DVR is now being used to evaluate the multi-dimensional integral, which is equivalent to using a quadrature procedure. The kinetic energy can also be evaluated by an analogous transformation of the FBR representation in Equation (17).

While Equation (18) is completely general, it is unsuitable for our requirements as it requires a transformation from the SPF basis to the full direct-product primitive grid. And this is precisely what the MCTDH method sets out to avoid as the full primitive grid for multi-dimensional systems has the dimensions of the standard wavepacket wavefunction discussed above. The advantages of the DVR can be used without the crippling scaling if the Hamiltonian is made up of products of functions with the same coordinates as the particles of the MCTDH wavefunction

$$H(q_1 \dots q_f) = \sum_{r=1}^{s} c_r h_r^{(1)}(Q_1) \dots h_r^{(p)}(Q_p). \tag{19}$$

The multi-dimensional integrals of Equation (18) are then reduced to products of low-dimensional integrals

$$\left\langle \varphi_{j_1}^{(1)} \dots \varphi_{j_p}^{(p)} \right| H \left| \varphi_{k_1}^{(1)} \dots \varphi_{k_p}^{(p)} \right\rangle = \sum_{r=1}^{n_s} c_r \left\langle \varphi_{j_1}^{(1)} \right| h^{(1)} \left| \varphi_{k_1}^{(1)} \right\rangle \cdots \left\langle \varphi_{j_p}^{(p)} \right| h^{(p)} \left| \varphi_{k_p}^{(p)} \right\rangle \tag{20}$$

and these low-dimensional integrals can be easily evaluated using the particle primitive grids which have the dimension N^d where d is the dimensionality of the particle.

An alternative approach that again avoids the use of the full primitive grid for the integrals, but does not require the product form of the potential is the CDVR method of Manthe [32]. This uses a time-dependent DVR to place suitable quadrature points and has been used with particular success by Manthe and co-workers to calculate rate constants of polyatomic molecules such as $CH_4 + H$ [33] $CH_4 + O$ [34].

Assuming the product representation of the Hamiltonian in Equation (19), the effort of MCTDH can be estimated by a sum of two terms:

$$\text{effort} \sim c_1 s p^2 n^{p+1} + c_2 s p n N^{2d} \tag{21}$$

where c_1 and c_2 are constants of proportionality. The first term is due to building the mean-field matrices and calculating the time-derivative of the A-coefficients. To build the mean-fields there are s terms in the Hamiltonian, and for each particle the A-coefficient vector must be multiplied by the Hamiltonian matrices for all the other particles. The time-derivative of the A-coefficients is obtained at the end of these operations for virtually no cost. The second term is due to the operation of the Hamiltonian on the SPFs, i.e. the operation of the s particle operators, represented in the particle primitive grids, on each SPF for each particle (for potential terms this becomes $spnN^d$ as the operator is diagonal in the primitive basis). The density matrices also need to be inverted, but this effort, which scales as n^3, is insignificant compared to these two terms.

Thus, if p is large, the effort for the algorithm is dominated by the building of the mean-field matrices. If p is small and d large the second-term, that for the propagation of the SPFs, dominates due to the high dimensionality of the functions. Again we see the trade between the effort required for the coefficients and the SPFs which can be altered by suitably combining DOFs together into particles, balancing the reduced effort due to low p with increased effort due to increasing N^d.

A final aspect of the MCTDH algorithm that affects its ability to efficiently solve the time-dependent Schrödinger equation is the ease of integration of the equations of motion. Wavepacket dynamics are an initial value problem. Starting from the wavepacket at $t=0$ it is propagated forward in time by integrating the equations of motion, which are written above as derivatives of the time. If the derivatives are smooth functions of time, then large time-steps can be taken. Unfortunately the MCTDH equations of motion are strongly coupled. All the sets of SPFs depend on each other on the A-coefficients through the mean-fields and the A-coefficients depend on the SPFs through the Hamiltonian matrix, $\boldsymbol{\mathcal{K}}$. The constant-mean-field integrator has been tailored to the properties of the method [3,35]. This uses the different evolution time-scales of the mean-fields and single-particle functions to separate the equations over a short time, and thus provide efficient integration.

2.3. *Multi-state calculations*

For non-adiabatic dynamics, systems have to be treated in which more than one electronic state is involved. Two different approaches have been used to include the electronic states. The first of these simply uses the equations of motion as written above, but with an extra DOF added to represent the electronic degree of freedom.

$$\Psi(q_1, \ldots q_f, \alpha, t) = \sum_{j_1=1}^{n_1} \cdots \sum_{j_p=1}^{n_p} A_{j_1 \ldots j_p}(t) \varphi_{j_1}^{(1)}(Q_1, t) \ldots \varphi_{j_{p-1}}^{(p-1)}(Q_{p-1}, t) \varphi_{j_p}^{(p)}(\alpha, t) \tag{22}$$

where α labels the electronic state. As a complete set of electronic SPFs is used in general, i.e. $n_p = \sigma$ where σ denotes the number of electronic states, the SPFs are time-independent and chosen as $\varphi_{j_p}^{(p)}(\alpha, t) = \delta_{\alpha, j_p}$. Introducing electronic state functions $|\alpha\rangle$ one may re-write the above equation as

$$\Psi = \sum_{j_1=1}^{n_1} \cdots \sum_{j_{p-1}=1}^{n_{p-1}} \sum_{\alpha=1}^{\sigma} A_{j_1 \ldots j_{p-1}, \alpha} \, \varphi_{j_1}^{(1)} \ldots \varphi_{j_{p-1}}^{(p-1)} \, |\alpha\rangle. \tag{23}$$

This is called the *single-set* formulation as one set of SPFs is used to treat the dynamics in all the electronic states.

In contrast, the *multi-set* formulation uses a different set of SPFs for each state. In this formulation, first introduced by Fang and Guo [36], one writes the wavefunction as

$$\Psi = \sum_{\alpha=1}^{\sigma} \Psi^{(\alpha)} \, |\alpha\rangle \tag{24}$$

where each component function $\Psi^{(\alpha)}$ is expanded in MCTDH form

$$\Psi^{(\alpha)}(q_1,\ldots,q_f,t)=\sum_{j_1^\alpha=1}^{n_1^\alpha}\cdots\sum_{j_p^\alpha=1}^{n_p^\alpha}A^{(\alpha)}_{j_1^\alpha\ldots j_p^\alpha}(t)\varphi^{(1,\alpha)}_{j_1^\alpha}(Q_1,t)\ldots\varphi^{(p,\alpha)}_{j_p^\alpha}(Q_p,t). \tag{25}$$

Note that different numbers of SPFs can be used for the different states, signified by the superscript α.

The equations of motion also now require state labels:

$$i\dot{\mathbf{A}}^{(\alpha)}=\sum_{\beta=1}^{\sigma}\mathcal{K}^{(\alpha\beta)}\mathbf{A}^{\beta}, \tag{26}$$

$$i\dot{\boldsymbol{\varphi}}^{(\kappa,\alpha)}=\left(1-P^{(\kappa,\alpha)}\right)\left(\boldsymbol{\rho}^{(\kappa,\alpha)}\right)^{-1}\sum_{\beta=1}^{\sigma}\boldsymbol{\mathcal{H}}^{(\kappa,\alpha\beta)}\boldsymbol{\varphi}^{(\kappa,\beta)}, \tag{27}$$

where the superscripts on the matrices denote that the matrix elements are with superscripted A-coefficients and SPFs. Thus, the particle Hamiltonian matrices used to build up the Hamiltonian matrix and mean-field operators are

$$\mathcal{K}^{(\alpha\beta)}_{JL}=\left\langle\Phi^{(\alpha)}_J\middle|H^{(\alpha,\beta)}\middle|\Phi^{(\beta)}_L\right\rangle \tag{28}$$

and

$$\mathcal{H}^{(\kappa,\alpha\beta)}_{ab}=\left\langle\Psi^{(\kappa,\alpha)}_a\middle|H^{(\alpha,\beta)}\middle|\Psi^{(\kappa,\beta)}_b\right\rangle \tag{29}$$

where $H^{(\alpha,\beta)}=\langle\alpha|\mathrm{H}|\beta\rangle$ denotes the (α,β) electronic component of the Hamiltonian. If $\alpha\neq\beta$ the matrices $\boldsymbol{\mathcal{K}}$ and $\boldsymbol{\mathcal{H}}$ are in general not square and non-Hermitian. The single set formulation requires fewer SPFs in total, and does not have to deal with the problem that the SPFs of different electronic states are not orthogonal to each other. In practice, however, the multi-set formulation has proved to be the more efficient as the SPFs adapt better to the different states and the total number of configurations required is less [37].

3. Photo-absorption spectra

Perhaps the easiest experimental observable to obtain is a photo-absorption spectrum. In the Condon approximation, which is appropriate for steady-state conditions with incident white light, the absorption spectrum, $\sigma(\omega)$ can be calculated from the Fourier transform of the autocorrelation function

$$\sigma(\omega)\propto\omega\int_{-\infty}^{\infty}\mathrm{d}t\,C(t)e^{i\omega t}, \tag{30}$$

where the autocorrelation function is defined as

$$C(t)=\langle\Psi(0)|\Psi(t)\rangle. \tag{31}$$

A detailed derivation is given in [38,39].

To obtain the autocorrelation function, the ground-state wavefunction is placed on the upper surface at the Franck–Condon point: "vertical excitation". This scheme is shown

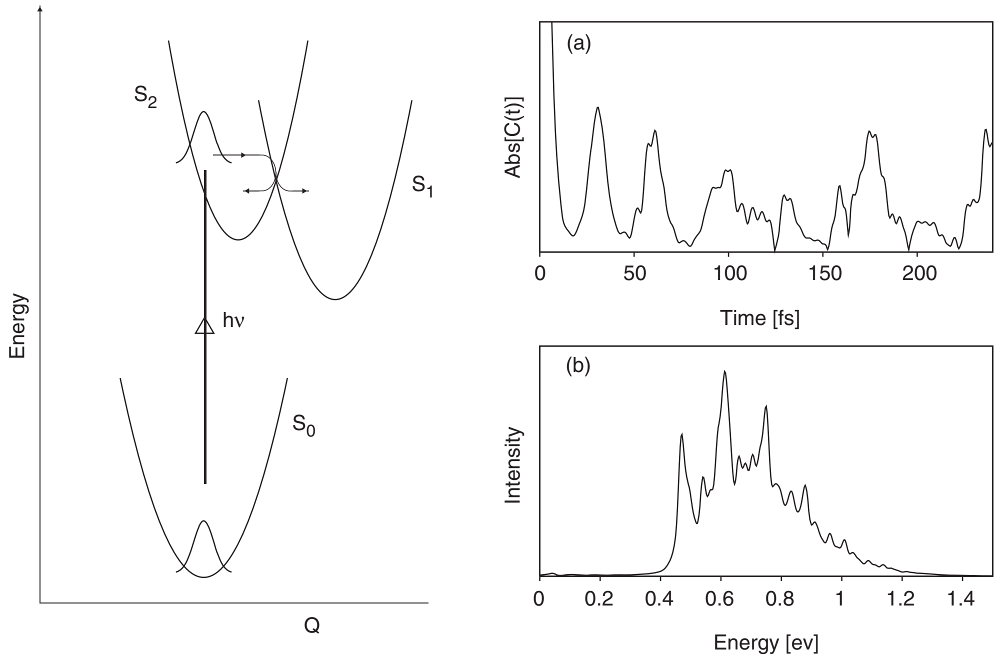

Figure 1. Scheme for the vertical excitation of a system from the S_0 state to S_2. The left panel shows the ground-state wavefunction projected into the manifold of excited states by the absorption of a photon. (a) An autocorrelation function and (b) the absorption spectrum calculated by the Fourier transform of the autocorrelation function.

in Figure 1 for the excitation from S_0 to S_2 of a system in which the upper state is coupled to a dark S_1 state. This assumes that the transition dipole moment is a constant with respect to the nuclear coordinates (Condon approximation). If this is not the case, the initial wavepacket needs to be multiplied by the transition dipole, which can be obtained from quantum chemistry calculations.

The wavepacket is then propagated on the excited state, i.e. it evolves under the influence of the excited-state Hamiltonian, and $C(t)$ is the overlap of the evolving function with its initial form. Greater efficiency can be obtained if the initial wavepacket is real and the Hamiltonian symmetric ($H = H^T$) as then [40,41]

$$C(2t) = \langle \Psi^*(t) | \Psi(t) \rangle, \tag{32}$$

i.e. the overlap of the wavefunction at time t with itself (not its complex conjugate) gives the autocorrelation function at time $2t$. This means that $C(t)$ is obtained over double the time of the propagation. This is a huge saving, not only directly due to the shorter propagation time, but also indirectly as shorter propagations require fewer SPFs. The initial wavefunction also does not need to be stored.

Spectra from the autocorrelation function have been obtained in a number of different systems such as photo-dissociation [40], photo-absorption [23], and photo-electron spectra [42]. Figure 1 shows the autocorrelation function and spectrum from a four-mode model used to investigate the photo-induced dynamics of pyrazine.

The main problem in obtaining spectra from the autocorrelation function is that the Fourier transform in Equation (30) goes to infinity, whereas the simulation time is finite. If $C(t) \rightarrow 0$ at large times, then there is no problem. This is the case in, e.g. photo-dissociation, but not in bound-state problems such as the example in Figure 1. To reduce errors due to the finite length, $C(t)$ can be multiplied by a damping function such as

$$g(t) = \cos\left(\frac{\pi t}{2T}\right)\Theta\left(1 - \frac{|t|}{T}\right) \tag{33}$$

where $\Theta(1 - (|t|/T))$ is the Heaviside function that switches from 1 to 0 at time T. This function smoothly forces $C(t)$ to be 0 at T. It has the effect of broadening the spectral lines. The autocorrelation function may additionally be multiplied by the factor

$$f(t) = \exp(-t/\tau). \tag{34}$$

This damping function is equivalent to convoluting the spectral lines with Lorentzian functions, the width of which can be related to a homogenous broadening due to experimental resolution [23].

4. State populations

For the interpretation of photo-chemical processes, the state populations as a function of time are often required. The population is given by the expectation value of the state projection operator

$$P_\alpha = \langle \Psi | \hat{P}_\alpha | \Psi \rangle = \langle \Psi | \alpha \rangle \langle \alpha | \Psi \rangle. \tag{35}$$

The electronic states can be defined using two different pictures: the *diabatic* and *adiabatic*. Both contain useful information. The former can be related to the electronic configurations of a molecule, while the latter are energy ordered states [7].

Wavepacket dynamics are usually performed in the diabatic picture, in which inter-state couplings appear in the Hamiltonian as potential-like terms. The diabatic populations are then straightforward to obtain. In the multi-set formulation the wavefunction has a component for each state, Equation (24). The population of state α is then the norm of this component

$$P_\alpha^{(d)} = \|\Psi^{(\alpha)}\|^2. \tag{36}$$

In the single-set formulation, Equation (22), the populations can be obtained from the density matrix for the electronic degree of freedom.

The adiabatic populations are not so easy to obtain. The diabatic and adiabatic wavefunctions are related by a position dependent unitary transformation

$$\mathbf{\Psi}^{(a)}(\mathbf{Q}) = \mathbf{U}(\mathbf{Q})\mathbf{\Psi}^{(d)}(\mathbf{Q}) \tag{37}$$

where the rotation matrix is given by the eigenvectors of the diabatic potential energy matrix at the point. This matrix transforms the diabatic potential matrix, **W**, to the diagonal adiabatic potential matrix, **V**

$$\mathbf{U}^\dagger(\mathbf{Q})\mathbf{W}\mathbf{U}(\mathbf{Q}) = \mathbf{V}(\mathbf{Q}). \tag{38}$$

Thus the projection operator for the adiabatic state α is

$$\hat{P}_{\alpha}^{(a)} = \sum_{\beta,\gamma} |\beta\rangle U^{\dagger}_{\beta\alpha} U_{\alpha\gamma} \langle\gamma|. \tag{39}$$

Unfortunately this operator does not have the MCTDH product-form because it is a complicated, non-separable function of the coordinates $\mathbf{Q}$. To avoid having to transform the wavefunction from the diabatic to adiabatic representation using the full primitive grid, one may use the *potfit* algorithm [3,43,44] to transform the projector to product form. This has been done successfully for a 6D model of ethene [45]. Unfortunately, this approach is limited to systems with no more than six or seven degrees of freedom, because the potfit algorithm needs to keep the function to be re-fitted – in general a potential but in this case $\hat{P}_{\alpha}^{(a)}$, the electronic matrix-element of the projector – in memory. For larger systems one has to turn to other, more approximate methods. Fortunately, the accuracy required for state populations is not high and so Monte Carlo integration can be used to solve the multi-dimensional integral in Equation (35). In [46] Monte Carlo integration was used to obtain adiabatic populations for a 14-dimensional system.

5. The vibronic coupling Hamiltonian

The vibronic coupling model adopted uses the well-known concept of diabatic electronic states [47–49]. Contrary to the usual adiabatic electronic states they are not – except for isolated points in nuclear coordinate space – eigenfunctions of the electronic Hamiltonian. Adiabatic electronic wavefunctions may have singular first derivatives with respect to the nuclear coordinates, e.g. at conical intersections of potential energy surfaces [6,7,12]. These important topological features have emerged as paradigms for non-adiabatic excited state dynamics [6,7,13,14]. They are thus difficult, if not impossible, to deal with in a quantum dynamics treatment in the adiabatic basis, because of diverging non-adiabatic – or derivative – coupling terms.

These singularities are removed by switching to a diabatic electronic basis using a suitable orthogonal transformation. This is thus the method of choice for quantum dynamics calculations. To be sure, the derivative couplings cannot be entirely removed in this way [50], but the remaining terms are non-singular and usually considered negligible for practical purposes. Also, for our purposes they are neglected, which may be considered as part of the model assumptions adopted. The potential coupling terms appearing instead in the diabatic basis are expanded in a low-order Taylor series in some suitable displacement coordinates. This constitutes the multi-mode vibronic coupling approach [12] which is used here. For the general case of n interacting electronic states we decompose the Hamiltonian into a kinetic and potential energy part, T_N and V_0, of some reference electronic state, and an $n \times n$ potential energy matrix $\mathbf{W}$, describing the changes in potential energy w.r.t. V_0 in the interacting manifold ($\mathbf{1}$ is the $n \times n$ unit matrix):

$$\hat{\mathbf{H}} = (T_N + V_0)\mathbf{1} + \mathbf{W}. \tag{40}$$

The matrix elements of **W** are written as follows:

$$W_{nn}(Q) = E_n + \sum_i k_i^{(n)} Q_i + + \sum_{i,j} \gamma_{ij}^{(n)} Q_i Q_j + \cdots \tag{41}$$

$$W_{nn'}(Q) = \sum_i \lambda_i^{(nn')} Q_i + \sum_{i,j} \mu_{ij}^{(nn')} Q_i Q_j + \cdots \quad (n \neq n'). \tag{42}$$

The truncation of the Taylor series after the first-order or second-order terms (the latter being shown here) is coined the linear or quadratic vibronic coupling approach (LVC or QVC, respectively) [6,7,12].

In typical applications we consider a photo-excitation or -ionization process where T_N and V_0 relate to the initial electronic state (usually the ground state), described in the harmonic approximation. The Q_i in Equation (41) are then the relevant dimensionless normal coordinates (harmonic frequencies ω_i) and we have

$$T_N = -\sum_i \frac{\omega_i}{2} \frac{\partial^2}{\partial Q_i^2}; \qquad V_0 = \sum_i \frac{\omega_i}{2} Q_i^2. \tag{43}$$

The quantities E_n appearing in Equations (41), (42) have the meaning of vertical excitation or ionization energies, referring to the centre of the Franck–Condon zone, $\mathbf{Q} = 0$ ($\mathbf{Q}$ denotes the vector of all coordinates). Because we take the diabatic and adiabatic basis states to coincide at this geometry, the E_n have no counterpart in the off-diagonal elements of Equation (42). The other parameters appearing in these expressions are called linear or quadratic coupling constants, in an obvious notation, either intra-state (for $n = n'$) or inter-state (for $n \neq n'$).

In molecules with symmetry elements, the latter can impose important restrictions on the modes appearing in the various summations of Equation (41), (42). These are relevant, in particular, for the linear coupling terms for which they read:

$$\Gamma_n \otimes \Gamma_Q \otimes \Gamma_{n'} \supset \Gamma_A. \tag{44}$$

Explicitly, a given vibrational mode with symmetry Γ_Q can couple electronic states with symmetries Γ_n and $\Gamma_{n'}$ in first order only if the direct product on the l.h.s. of Equation (44) comprises the totally symmetric irreducible representation Γ_A of the point group in question. The generalization to the second-order terms should be apparent, though it is less restrictive. From Equation (44) one immediately deduces (given an Abelian point group) that for $n = n'$ only totally symmetric modes enter the Hamiltonian in first order. Thus – for electronic states of different symmetries – the intra-state and inter-state linear couplings are caused by different sets of modes [12]. This will indeed be the case for the examples below, as far as Abelian point groups are concerned. For non-Abelian point groups there may be electronic states degenerate by symmetry, and the above discussion has to be suitably generalized. That is, the direct product $\Gamma_n \otimes \Gamma_n$ has to be replaced by its symmetric counterpart [51,52], and the indices appearing in Equations (41), (42), should be extended to cover also the various components of degenerate irreducible representations. Consequently, also non-totally symmetric modes may appear in the diagonal elements of Equation (41) in first order. This amounts to the Jahn– Teller effect which is dominated by symmetry restrictions even more than for the case of Abelian point groups discussed above. For details we refer to the large amount of literature in the field [51,52].

Despite the importance of the diabatic basis for dynamical calculations, the adiabatic representation is useful at least in two different respects. First, the key features of the adiabatic potential energy surfaces, such as minima of crossing seams, double minima occurring at a reduced symmetry, etc. are vital to interpreting essential features of the nuclear dynamics such as spectra and electronic populations [6,12]. Second, the adiabatic surfaces are also needed to determine the various coupling constants entering Equations (41), (42) from *ab initio* electronic structure calculations. The latter necessarily give adiabatic quantities, at least in a direct sense. The comparison of the adiabatic surfaces underlying Equations (41), (42) with *ab initio* results thus allows the parameters such as coupling constants to be determined by requiring that the corresponding model surfaces reproduce the *ab initio* data as well as possible.

For the linear intra-state couplings particularly simple expressions can be given [12], since these are just the gradients of the potential energy surface with respect to the normal coordinates of the modes in question:

$$k_i^{(n)} = \left(\frac{\partial V_n}{\partial Q_i}\right)\bigg|_{\mathbf{Q}=\mathbf{0}}. \tag{45}$$

Similarly, for a two-state problem with a non-totally-symmetric active mode (coordinate Q_u, frequency ω_u), the parabolic-plus-hyperbolic shape of the resulting adiabatic potential curves V_1 and V_2 [12]

$$V_{1,2} = (E_1 + E_2)/2 + \omega_u Q_u^2/2 \pm \sqrt{(E_1 - E_2)^2/4 + (\lambda Q_u)^2} \tag{46}$$

readily gives the following expression for the inter-state coupling constant:

$$\lambda = \sqrt{\frac{1}{8}\frac{\partial^2 (V_1 - V_2)^2}{\partial Q_u^2}\bigg|_{\mathbf{Q}=\mathbf{0}}}. \tag{47}$$

In more general situations, such as three states interacting through the same vibrational mode, the coupling constants may be determined by a least-squares fit of the model eigenvalues to electronic structure data [53]. A general fitting procedure for any size of system is also described below in Section 7.

We conclude this section by pointing out that the model nature of the Hamiltonian, Equations (41), (42), and its potential energy surfaces, apparently introduces restrictions on the type of problem to be treated, e.g. photo-chemical transformations [13,14]. More recently, an extension has been proposed and successfully applied, where the model has been used only for the adiabatic-to-diabatic mixing angle [6]. This so-called concept of regularized diabatic states [54–56] allows the treatment of general potential energy surfaces, but at the expense of losing the structural simplicity of the Hamiltonian. As pointed out above, and will become further apparent below, it is this structural simplicity, where all operators entering the Hamiltonian are simple products of the coordinates, which brings the MCTDH algorithm to full power. This would apparently no longer be the case with general potential energy surfaces appearing within the concept of regularized diabatic states. Therefore, in the applications presented below, we use the vibronic model in the original, direct form as expressed by the Hamiltonian (40)–(42). Despite the restricted form it will become clear below that the model covers a rich variety of phenomena and can be applied to truly multi-dimensional problems.

6. Combining the vibronic coupling model with MCTDH

Perhaps the easiest way to show why MCTDH and the vibronic coupling model Hamiltonian fit so well together is to look at an example. The calculation that really proved the potential of the MCTDH method was the calculation of the absorption spectrum of pyrazine explicitely including all 24 vibrational modes [23]. The first two bands of the absorption spectrum of this molecule provide a classic example of a conical intersection. The lower band has a well-defined vibrational structure, as expected for a bound state. The upper band is intense and fairly featureless [57]. This lack of structure was shown to be due to a conical intersection between the S_1 and S_2 states, which results in the short lifetime in the upper electronic state [58].

The pyrazine molecule has 24 vibrational modes. Its equilibrium geometry has a point group D_{2h} and the coupled S_1 and S_2 states have B_{3u} and B_{2u} symmetry respectively. Thus, the quadratic vibronic coupling model Hamiltonian can be written

$$\begin{aligned}\hat{\mathbf{H}} = {} & \sum_i \frac{\omega_i}{2}\left(-\frac{\partial^2}{\partial Q_i^2}+Q_i^2\right)\mathbf{1} + \begin{pmatrix}-\Delta & 0\\ 0 & \Delta\end{pmatrix} + \sum_{i\in G_1}\begin{pmatrix}\kappa_i^{(1)} & 0\\ 0 & \kappa_i^{(2)}\end{pmatrix}Q_i \\ & + \sum_{(i,j)\in G_2}\begin{pmatrix}\gamma_{i,j}^{(1)} & 0\\ 0 & \gamma_{i,j}^{(2)}\end{pmatrix}Q_iQ_j + \sum_{i\in G_3}\begin{pmatrix}0 & \lambda_i\\ \lambda_i & 0\end{pmatrix}Q_i + \sum_{(i,j)\in G_4}\begin{pmatrix}0 & \mu_{i,j}\\ \mu_{i,j} & 0\end{pmatrix}Q_iQ_j \qquad (48)\end{aligned}$$

where G_1 are the five symmetric modes that appear linearly on the diagonal and G_3 the b_{1g} mode that provides linear coupling between the two states. G_2 are the pairs of modes whose product is totally symmetric and so appear with quadratic and bilinear terms on the diagonal, and finally G_4 are the pairs of modes whose product has symmetry b_{1g} and thus provide bilinear coupling terms.

A four-mode model, including the coupling mode ν_{10a} and three of the a_{1g} modes, ν_{6a}, ν_1 and ν_{9a}, was shown by Domcke and co-workers to be able to reproduce the features of the S_2 spectrum using standard wavepacket dynamics calculations [58]. The envelope, however, was only reproduced by adding a phenomenological broadening to the spectrum, damping the autocorrelation function with a fast relaxation time of 30 fs. This must be due to the coupling between the four-mode 'system' and the 'bath' provided by the remaining 20 modes.

A simple model coupling the four-mode system to a 20-mode bath was set up and studied using a path integral method [59] and later MCTDH [37]. This used the correct pyrazine mode frequencies but suitably chosen linear coupling constants and could not reproduce the measured spectrum. For this, a full calculation requires the model to be correctly extended to second order, including the coupling as quadratic and bilinear terms.

The 174 parameters required for the second-order model were calculated by Raab *et al.* [23] using the simplest possible method for calculating electronic states: configuration interaction with single excitations (CIS). The spectrum was then obtained from the Fourier transform of the autocorrelation function (see Section 3), calculated using the

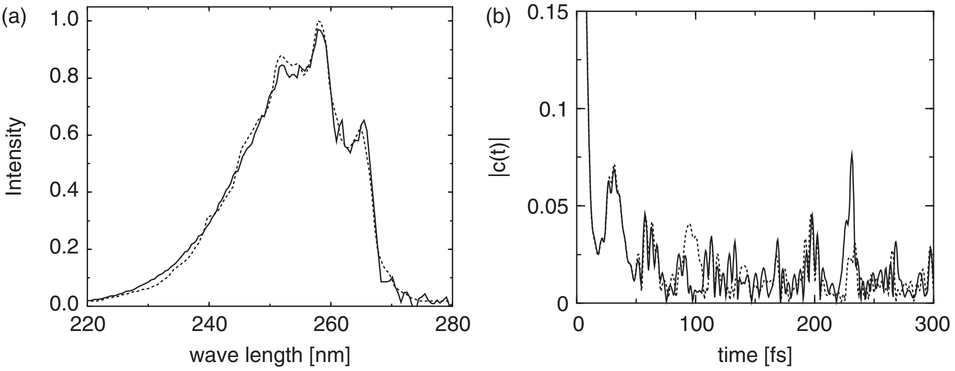

Figure 2. The absorption spectrum of pyrazine. (a) The experimental spectrum (dashed line) compared to that calculated using a 24-mode vibronic coupling model Hamiltonian and the MCTDH method with a large basis set (full line). (b) The calculated absolute value of the pyrazine autocorrelation function from two 24-mode MCTDH calculations using different basis sizes. Large basis set (full line), small basis set (dashed line). See Table. 1 for details.

MCTDH method. After minor adjustment of key parameters, the agreement with the experimental spectrum is seen to be very good (Figure 2a). Note that a small, 150 fs, damping has been added to the autocorrelation function to produce this spectrum to allow for the finite propagation time of the simulation.

The power of the MCTDH method can be seen in the fact that this calculation was at all possible using the available hardware in 1999. The technical details of the basis sets used are summarized in Table 1. The rows correspond to different models studied: the Domcke four-mode model; a 12-mode model that augments these four-modes with the remaining 8-modes with g-symmetry; the full 24-mode system. Two 24-mode calculations are listed with different numbers of SPFs. The second column details how the degrees of freedom were combined together to form multi-dimensional ‘particles’. As discussed in Section 2.2, this keeps the length of the wavefunction expansion short. The four-mode calculation used four one-dimensional particles, i.e. four sets of one-dimensional functions were used as the SPFs. The 12-mode calculation used five particles with, for example, the ν_{10a} and ν_{6a} combined together to give a 2D particle. The 24-mode calculation used eight particles.

The wavefunction expansion length is the total SPF basis size, given by the product of the number of SPFs per particle, summed over the two states. The numbers are given in column 3. For the four-mode and 12-mode calculations the expansion length is 10,720 and 45,240 respectively. For the two 24-mode calculations, calculation I has a length of 502,200 and calculation II 2,771,440. The four-mode and 12-mode are both converged with respect to the autocorrelation function, and hence the spectrum. A full test of convergence could not be made for the 24-mode calculations, but the number of SPFs for 24-mode II were chosen so that the population of the highest natural orbital was less than 0.01, suitable for averaged quantities. A comparison with the smaller 24-mode I calculation supports this. The autocorrelation function is shown in Figure 2(b) and the all important first two peaks are nearly identical.

Table 1. Technical details of the MCTDH calculations of the absorption spectrum of pyrazine Ref. [23]. The round brackets denote the combination of vibrational modes, the square brackets the number of SPFs used for the representation of the wavefunction in the S_1 and S_2 states. The number of modes in one combination define the dimensionality of the corresponding SPFs. These SPFs are represented on a grid whose size is given by the product of the number of grid points used for each mode of the corresponding combination.

Model	Combination of modes	Number of grid points	Number of SPFs $[S_1, S_2]$
4 mode	$\nu_{10a}, \nu_{6a}, \nu_1, \nu_{9a}$	40, 32, 16, 12	[10,8], [16,10], [7,6], [7,6]
12 mode	$(\nu_{10a}, \nu_{6a}), (\nu_1, \nu_{9a}),$ $(\nu_2, \nu_{6b}, \nu_{8b}), (\nu_4, \nu_5)$ $(\nu_{7b}, \nu_{8a}, \nu_3)$	(40, 32), (20, 12), (4, 12, 24), (24, 8), (4, 8, 12)	[14,11], [10,8], [6,6], [7,6], [5,5]
24 mode I	$(\nu_{10a}, \nu_{6a}), (\nu_1, \nu_{9a}, \nu_{8a}),$ $(\nu_2, \nu_{6b}, \nu_{8b}), (\nu_4, \nu_5, \nu_3),$ $(\nu_{16a}, \nu_{12}, \nu_{13}), (\nu_{19b}, \nu_{18b}),$ $(\nu_{18a}, \nu_{14}, \nu_{19a}, \nu_{17a}),$ $(\nu_{20b}, \nu_{16b}, \nu_{11}, \nu_{7b})$	(40, 32), (20, 12, 8), (4, 8, 24), (24, 8, 8), (24, 20, 4), (72, 80), (6, 20, 6, 6) (6, 32, 6, 4)	[12,9], [6,5], [4,3], [5,3] [4,3], [6,6] [4,4], [3,3]
24 mode II	same as I	same as I	[14,11], [8,7], [6,5], [6,4], [4,5], [7,7], [5,5], [3,4]

The SPFs need to be described by a primitive basis set. For this, a harmonic oscillator DVR basis was used [3], which has been found to be very efficient for such bound-state problems. The number of functions required for each degree of freedom are given in column 4. Thus, 40 DVR functions were used for the ν_{10a} mode, 32 for the ν_{6a} mode, etc. The primitive basis size for each particle is given by the bracketed numbers so, for example, the primitive basis size of the 2D particle containing the ν_{10a} and ν_{6a} modes in the 12-mode calculation is 1280. For efficiency, it is important to keep the primitive basis sizes for the various particles similar in length.

The total primitive basis, that which would be required in a standard wavepacket calculation, is given by the product of the number of grid points for all modes. For the four-mode, the 12-mode and the 24-mode problems these were, respectively: 245,760; 2.6×10^{13}; and 6.4×10^{26}. The contraction efficiency of the MCTDH method is then the ratio of the MCTDH wavefunction expansion length to the primitive basis size. For these large calculations the expansion length is clearly a much smaller number than the primitive basis.

Finally, we should mention the resources required for these calculations. For propagation lengths of 150 fs, the four-mode calculation required only 20 minutes on an IBM RS/6000 workstation and 16 MB memory. Very cheap for a full four-dimensional quantum dynamics calculation. For the 12-mode calculation on the same machine, this rose to 10 hours and 45 MB memory. For the large 24-mode II calculation, a CRAY T90 vector machine was used and 485 hours of CPU-time was required with 650MB memory. This is a substantial, but manageable amount of time. The power of the method again can be seen in that the smaller, 24-mode I, calculation required only 100 hours and 205 MB to

Table 2. Calculations on non-adiabatic systems using the MCTDH method in combination with the vibronic coupling model Hamiltonian. f is the number of nuclear degrees of freedom and s the number of electronic states included in the calculations.

Molecule	Phenomenon	f	s	Ref.
Pyrazine	System-bath IVR	24	2	[46,108]
Pyrazine	Absorption spectrum	24	2	[23]
Allene	Photo-electron spectrum	15	3	[42]
Benzene	Photo-electron spectrum	13	5	[76]
Pentatetraene	Photo-electron spectrum	21	5	[71]
$Cr(CO)_6$	Photo-dissociation mechanism	5	3	[73]
Cyclobutadiene	Photo-electron spectrum	6	3+2	[109]
Benzene	Time-resolved photo-electron spectrum	3	4	[26]
Butatriene	Photo-electron spectrum	18	2	[68,92]
Ozone	Photodissociation	3	2	[110]
Furan	Absorption spectrum	13	4	[111]
Cyclopropane	Photo-electron spectrum	14	4	[112]

produce a spectrum that is of a good quality. Today, as they require less than 1 GB of memory, all these calculations can be done on a desktop PC.

7. Examples

A number of systems have been treated using the vibronic coupling model. The first was the butatriene cation [10]. In this molecule, the first excited-state has ${}^2B_{2u}$ symmetry and non-adiabatic coupling to the ${}^2B_{2g}$ ground-state takes place via the torsional mode, which has a_u symmetry. This leads to a conical intersection between the two states, the presence of which is responsible for the 'mystery band' seen in the photo-electron spectrum between the bands expected for the states [60]. The systems treated using the MCTDH method, which include the butatriene cation, are listed in Table 2. The table shows the property studied, and the size of the model used. Below, a few calculations are looked at to demonstrate the work.

7.1. *Allene cation*

The calculation of the pyrazine absorption spectrum detailed above showed the importance of including second-order terms for a complete treatment. A further example where second-order terms must be included into the model to correctly describe a spectrum is found in the photo-electron spectrum of allene. The equilibrium structure of allene has the point group D_{2d}. Doubly degenerate states of the ion, labelled ${}^2E$, are thus subject to $E \otimes \beta$ Jahn–Teller coupling, where the symmetry of the state is lowered by coupling to pairs of modes, one with B_1 and one with B_2 symmetry. The $\tilde{A}^2E$ state is further pseudo-Jahn–Teller coupled to the $\tilde{B}^2B_2$ state via the doubly degenerate E modes.

The photo-electron spectrum [61] for this coupled band shows a well-structured lower energy portion that could be explained by the Jahn–Teller coupled $\tilde{A}$ band with progressions from one symmetric stretch and a pair of Jahn–Teller active modes [62,63].

Later work then assigned the diffuse higher part of the spectrum to the pseudo-Jahn–Teller coupled system [64]. However, the assignment of the lower part of the spectrum was found to be incompatible with the coupling when looking at all the possible modes as there are three strongly coupled modes with relevant frequencies. The answer was that the second-order coupling between these modes leads to significant changes in the frequencies by what is termed Duschinsky rotation. A simulation with all 15 modes and three states, while still not in perfect agreement with experiment, supports this [42].

An interesting feature of the allene cation system is that the the doubly-degenerate ground state wavefunction can be written so that each component has a hole at different ends of the molecule. This molecule thus provides an interesting model for charge transfer along a conjugated chain – starting in one component of the ground-state is equivalent to removing an electron from one end of the molecule. Population transfer between the components then monitors the transfer. Due to the vibronic coupling this is found to be an ultrafast process [65].

The problem when including second-order terms is not only the increase in system size, but also the number of parameters that need to be determined. The linear model for pyrazine has 13 parameters and the second-order model 174. Similarly, the linear model for allene has 25 parameters and a further 16 second-order parameters, thought to be the most important, were added from the many possible. In these examples, the parameters were calculated by hand from information obtained at a few points on the potential energy surfaces using the formulae given in Section 5. This quickly becomes a very laborious task for more modes, especially if many states are involved.

To deal with this fitting problem, an automated scheme has been set up and implemented as the VCHAM program [66], which is distributed with the MCTDH package [67]. This was first used to calculate the 79 parameters in a quadratic model of the butatriene cation [68]. The program sets up appropriate geometries for calculating the energies along cuts through the potential surfaces, collates the information, and then fits the parameters so that the model matches the calculated adiabatic surfaces. In a recent example, the VCHAM procedure has been used to obtain parameters for a vibronic coupling model of the lowest six excited states of benzene at the CASSCF level, revealing the different types of coupling present in these states [69]. Going to a quadratic model, which is necessary in this case for a good fit, requires a large number of parameters which are not independent.

The allene radical cation demonstrate the utility of this approach. The surfaces for the $\tilde{A}^2E/\tilde{B}^2B_2$ coupled states, together with the $\tilde{C}^2A_1$ have been studied [70]. All four states are required for a good fit. Furthermore, it was found during the fitting process that satellite states also had to be included to get the form of the potentials along the low frequency doubly degenerate modes that are important in the pseudo-Jahn–Teller coupling. Fourth-order terms were also required along some modes. The procedure also allowed the use of electronic structure methods for which analytic gradients are not available as only single-point energies are required.

The quality of the fits along the most important modes is shown in Figure 3. It is clear that despite the simplicity of the model, it is able to describe the anharmonicity of the adiabatic surfaces extremely well. The model for the related, but larger, pentatetraene system has also been calculated and used to interpret the experimental spectrum [71].

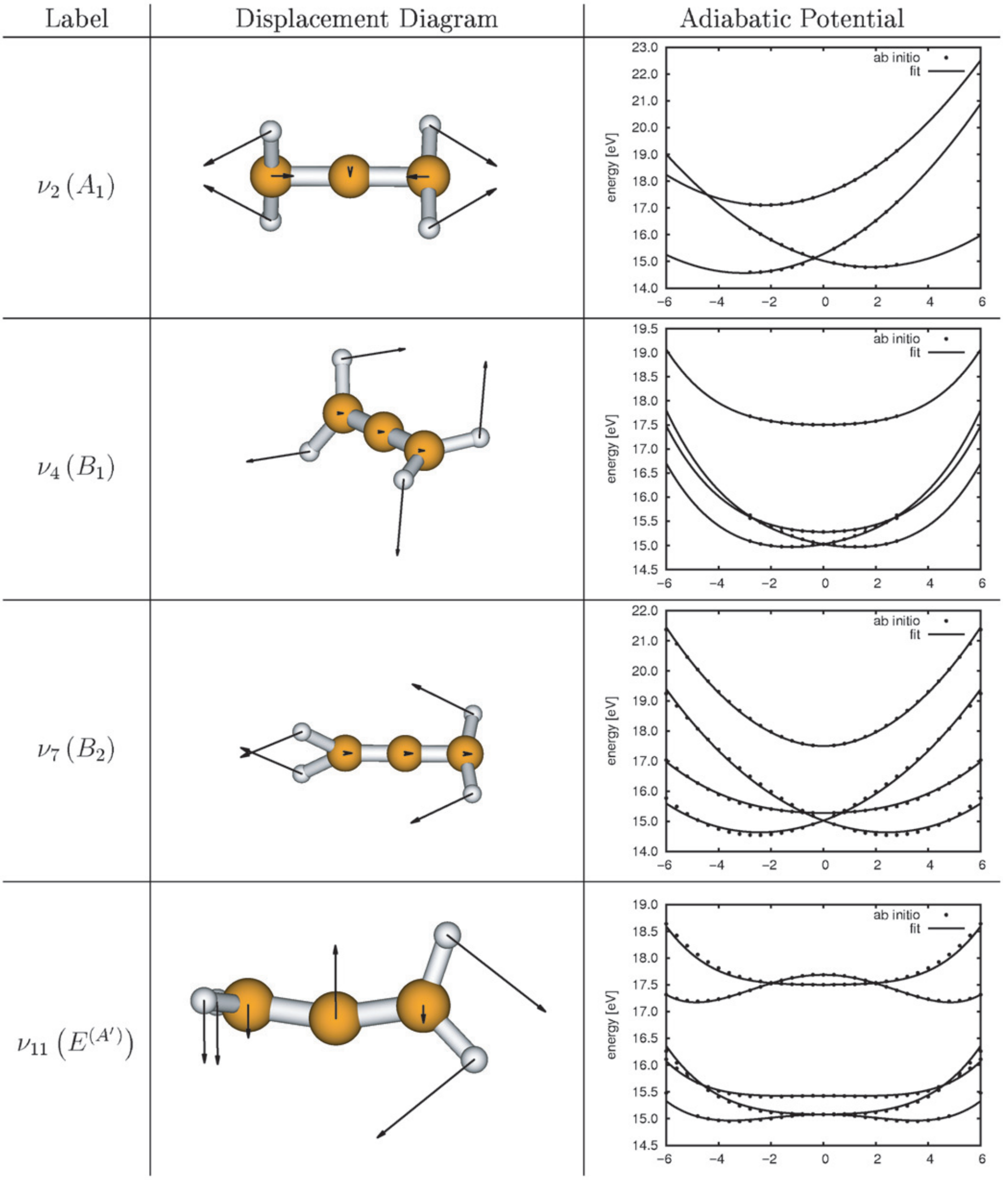

Figure 3. [Colour online] Cuts through the PES of allene along normal modes important for the non-adiabatic dynamics. The potentials show the data from *ab initio* calculations as points. The lines are the adiabatic surfaces from the vibronic coupling model Hamiltonian. Taken from [70].

7.2. *Cr(CO)$_5$*

By not focusing on just the intersection region, the VCHAM fitting procedure also allows a better analysis of the global surfaces, and can lead to new findings. For example, the ground-state adiabatic surface of Cr(CO)$_5$ shows the moat and three minima typical of a second-order Jahn–Teller interaction in the ground-state that is doubly degenerate at D_{3h} geometries [72]. On fitting the surfaces globally, however, the topology was actually found to be predominantly due to an $(E \oplus A) \otimes e$ pseudo-Jahn–Teller interaction between the ground state and the lowest singly degenerate excited state [73]. The dynamics in a pseudo-Jahn–Teller system are distinct from those in a Jahn–Teller system: in the latter a wavefunction propagated on the lower adiabatic surface is subject to the geometric phase effect while in the former it is not [74]. This has consequences for the shape of the evolving wavepacket.

Calculations were performed using the three-states and the five most important vibrations, namely the two doubly-degenerate pairs that account for both the Jahn–Teller and the pseudo-Jahn–Teller coupling in addition to the symmetric breathing mode. The dynamics after forming the $Cr(CO)_5$ molecule by photo-dissociation is shown in Figure 4. The results of two calculations are shown: including just the two strongest coupling modes, and including the five most important. The calculation of the adiabatic populations of the five-mode model is a huge job – requiring the multi-mode transformation operator on the full primitive grid (see Section 4) which has 3.3×10^{11} points. A Monte Carlo integration scheme was used for this.

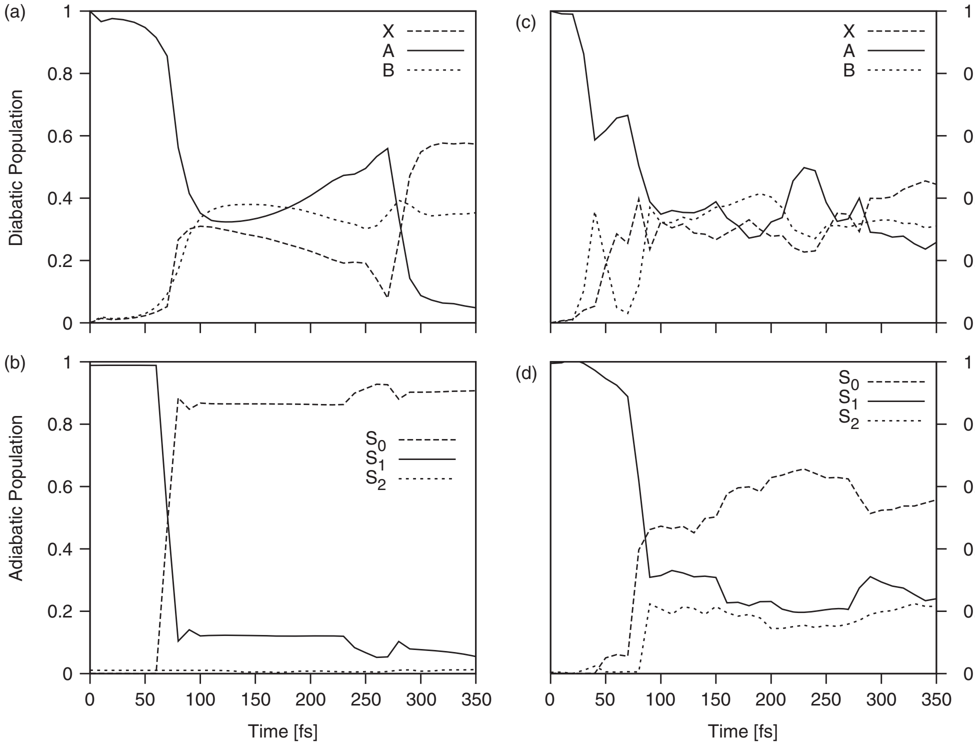

Figure 4. State populations of $Cr(CO)_5$ after formation in the Ã state by photo-dissociation of $Cr(CO)_6$. The model included the lowest three electronic states and the most strongly coupled modes. (a) The diabatic state populations and (b) adiabatic state populations including only two modes. (c) The diabatic state populations and (d) adiabatic state populations including five modes.

The diabatic populations represent the population of the states with electronic wavefunctions dominated by chromium d-electron configurations $\Phi_{\tilde{X}} = d_{xz}^2 d_{yz}^2 d_{xy}^2$, $\Phi_{\tilde{A}} = d_{xz}^2 d_{yz}^2 d_{xy}^1 d_{x^2-y^2}^1$ and $\Phi_{\tilde{B}} = d_{xz}^2 d_{yz}^2 d_{x^2-y^2}^2$, respectively. The system starts in the diabatic $\tilde{A}$ state. In the two-mode calculation, after 100 fs there is a large transfer of population to both the other states. After another 150 fs there is a further transfer, after which little is left in the initial state. The transfer is similar, but less smooth in the five-mode calculation. Earlier transfer is also seen and the second transfer is weaker due to the spreading of the wavepacket in the larger available space reducing the effect of the recurrence.

The adiabatic states in this system are effectively $\Phi_{S_1} = \Phi_{\tilde{X}} - \Phi_{\tilde{B}}, \Phi_{S_2} = \Phi_{\tilde{A}}$, and $\tilde{\Phi}_{S_3} = \Phi_{\tilde{X}} + \Phi_{\tilde{B}}$. In these states, the population transfer in the two-mode model is more dramatic: it is effectively finished after 100 fs, having transferred 90% of the population to the ground-state. In the five-mode model, the transfer out of S_2 is less, and the S_3 state becomes more populated.

Figure 5 plots snapshots of the adiabatic wavepacket motion over the ground and first-excited states for this system. The plot is in the space of the doubly-degenerate vibrational mode that has the strongest coupling. The PESs for the lowest two adiabatic states are shown in the figure, with three minima on the lower state at C_{4v} symmetry, and three narrow minima on the upper state all due to the pseudo-Jahn–Teller coupling between the three diabatic states. The intersection between the states is at the centre of the plot at the D_{3h} geometry. This plane corresponds to pseudo-rotation of the molecule: moving from minima to minima corresponds to a rearrangement of the three equatorial carbonyl groups [72].

The dynamics start on the first adiabatic excited state with a C_{4v} structure, distorted along the Q_2 mode. This initial condition is that formed by the sudden removal of a single carbonyl group and the wavepacket at this time is taken to have the form of the undisturbed ground-state vibrational eigenfunction for the vibrations. After 80 fs the wavepacket has reached the D_{3h} geometry and population transfer to the ground-state takes place. This bifurcates and returns to the D_{3h} centre after 240 fs. There is a small recurrence to the upper state seen in the adiabatic populations at this time. Finally, the wavepacket on the ground-state reaches the right-hand side of the well after 340 fs. This time-scale fits the time-scale of coherent motion measured by Trushin *et al.* for this system [75]. Note that the wavepacket on the ground-state in Figure 5 is symmetrical, in contrast to the plot in the original paper (Figure 8 in [73]). This was due to a plotting error in the analysis.

7.3. *Benzene cation*

The ability to follow the dynamics in a manifold of coupled states is exemplified by calculations on the benzene cation [53,76]. The photo-electron spectrum of benzene has a number of bands in the region 9–20 eV [77]. The surfaces for the lowest five bands (8 states) have been fitted using the linear vibronic coupling model [53]. These states are all vibronically coupled and Figure 6 shows the coupling along an effective mode.

Large MCTDH calculations have shown that the model is able to reproduce the experimental spectrum [76]. These then allow a detailed analysis of the modes important for the system dynamics. Figure 7 shows the state populations after starting in the non-degenerate $\tilde{C}$ state. The modes required are the symmetric breathing mode and the doubly degenerate modes with e_{2g} symmetry that provide the Jahn–Teller coupling within

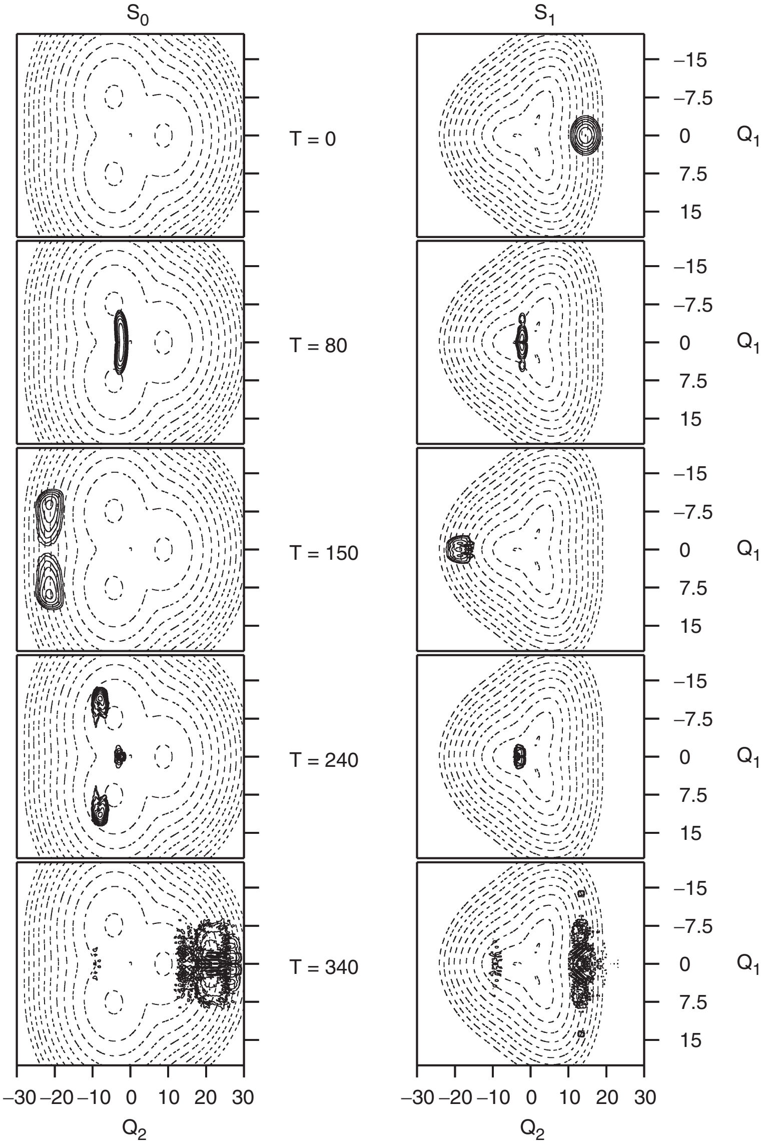

Figure 5. Snapshots of the adiabatic wavepacket of $Cr(CO)_5$ after formation from the photodissociation of $Cr(CO)_6$. The right-hand panel shows the upper, S_1, state and the left-hand panel the lower, S_0. The dotted lines are contours representing the adiabatic potential energy surfaces. The full contours represent the wavepacket density. The coordinates are the strongest coupling doubly degenerate modes.

the $\tilde{X}$ and $\tilde{B}$ states. The pseudo-Jahn–Teller coupling between the $\tilde{B}$ and $\tilde{C}$ states is provided by modes with e_{2u} symmetry, that between the $\tilde{X}$ and $\tilde{B}$ states by modes with b_{2g} symmetry. An effective mode was used to model the coupling provided by the pair of modes with this symmetry.

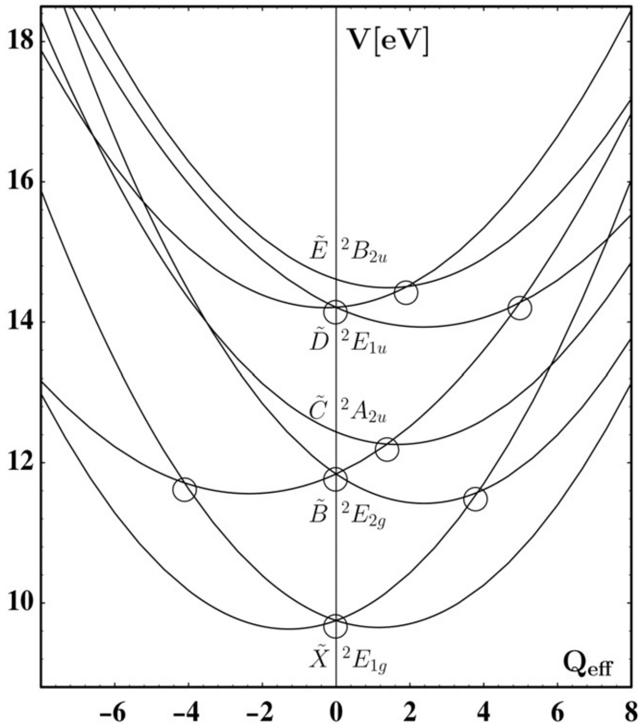

Figure 6. A schematic diagram of the lowest eight electronic states in the benzene radical cation shown as a cut along an effective mode. Conical intersections between the states are circled.

The population is seen to decay rapidly from the $\tilde{C}$ state and after 200 fs the population is shared equally by the $\tilde{B}$ and $\tilde{X}$ states. Initial transfer occurs to the $\tilde{B}$ state, followed by transfer to the ground-state. Similar results were obtained ignoring the degeneracy of the modes (Figure 7b). These findings are of relevance for the fluorescence dynamics of the benzene cation. They provide a pathway for ultrafast $\tilde{C} \longrightarrow \tilde{X}$ non-radiative relaxation, and thus explain the absence of emission in this system. Similar calculations have also been performed for the higher excited states of Figure 6 and have been related to the fragmentation dynamics of the cation [78]. Finally, the studies have been extended to the monofluoro derivative [79,80] and also the three difluorobenzene isomers [81] and the characteristic changes observed experimentally for fluorination been reproduced and interpreted in this way.

8. Parameterized basis functions: G-MCTDH

In the G-MCTDH method [27] the configurations for the wavefunction ansatz Equation (1) are written

$$\Phi_J(Q_1,\ldots,Q_p,t) = \prod_{\kappa=1}^{m} \varphi_{j_\kappa}^{(\kappa)}(Q_\kappa,t) \prod_{\kappa=m+1}^{p} g_{j_\kappa}^{(\kappa)}(Q_\kappa,t) \tag{49}$$

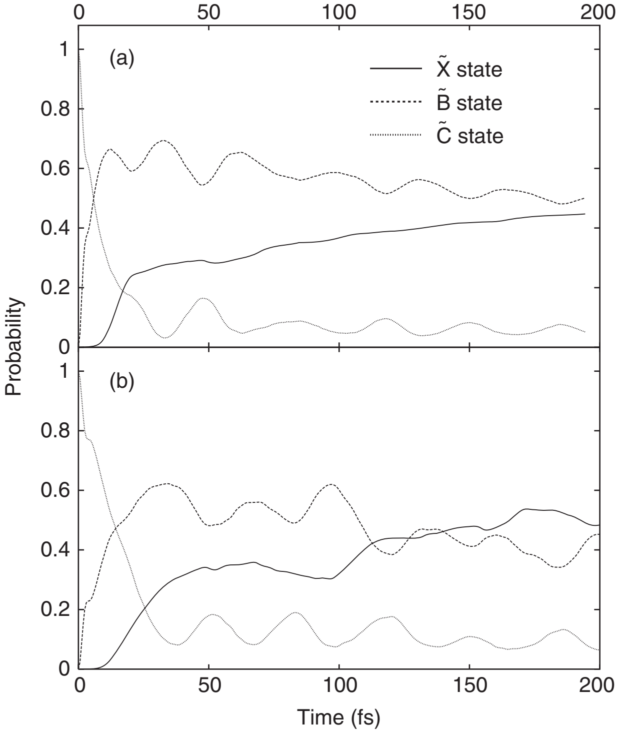

Figure 7. The population dynamics of the $\tilde{X}-\tilde{B}-\tilde{C}$ system of the benzene radical cation. (a) The symmetric mode ν_2 along with the degenerate modes ν_{16}, ν_{18} and ν_{19} (Herzberg numbering) as well as an effective mode with b_{2g} symmetry were included along with all five electronic states. The populations of $\tilde{B}$ and $\tilde{X}$ are the sum of the two components. (b) The same calculation, but treating all modes and states as non-degenerate (five modes and three states). Taken from [76].

where the first m particles are described by the flexible SPFs described above which are expressed using the primitive basis functions, and the remaining particles are described by SPFs which are defined using a small number of parameters. The idea is that by propagating a limited set of parameters rather than the functions themselves a huge saving of memory can be made. Part of the system can be treated using the usual grid-based wavepacket methods described above, and part using the parameterized functions. As the latter may introduce approximations into the dynamics, in this way a system can be described using a hierarchy of modes with a 'full quantum-mechanical' part coupled to an 'approximate quantum-mechanical' part.

While the method is completely general, and any parametrized form could be used, a simple and suitable form is the Gaussian:

$$g_j^{(\kappa)}(\mathbf{Q}_\kappa, t) = \exp[\mathbf{Q}_\kappa \cdot \zeta_j^{(\kappa)}(t) \cdot \mathbf{Q}_\kappa + \xi_j^{(\kappa)}(t) \cdot \mathbf{Q}_\kappa + \eta_j^{(\kappa)}(t)]. \tag{50}$$

The parameterized functions are thus referred to as Gaussian Wavepackets (GWPs). Both 'thawed' Gaussians (with a time-dependent width matrix, $\zeta_j^{(\kappa)}(t)$) and 'frozen' Gaussians (with a fixed width) have been employed [82,83]. In numerical applications, however, frozen Gaussians are found to be more robust. In the limit that only GWPs are used to describe the wavefunction, the method is termed the *variational multi-configurational Gaussian wavepacket* (vMCG) method.

Equations of motion can be set up using the variational principle as before. The main changes to those for the flexible SPFs and A-coefficients are due to the non-orthonormality of the GWPs. Defining the particle GWP overlap and time-derivative overlap matrices as

$$S_{ij}^{(\kappa)} = \left\langle g_i^{(\kappa)} \middle| g_j^{(\kappa)} \right\rangle \tag{51}$$

$$\tau_{ij}^{(\kappa)} = i\left\langle g_i^{(\kappa)} \middle| \dot{g}_j^{(\kappa)} \right\rangle \tag{52}$$

and using a configuration overlap matrix

$$\mathcal{S}_{IJ} = \left\langle \Phi_I \middle| \Phi_J \right\rangle \tag{53}$$

the equation of motion for the A-coefficients can be written

$$i\dot{\mathbf{A}} = \boldsymbol{\mathcal{S}}^{-1}\left(\boldsymbol{\mathcal{K}} - \sum_\kappa \boldsymbol{\tau}^{(\kappa)}\right)\mathbf{A}\,. \tag{54}$$

The equations for the SPFs are unchanged, but it should be noted that the density matrix elements contain the overlap matrices and Equation (11) must be accordingly re-written. Finally, the equations of motion for the GWP parameters can be written

$$i\dot{\boldsymbol{\Lambda}}^{(\kappa)} = \left[\mathbf{C}^{(\kappa)}\right]^{-1} \mathbf{Y}^{(\kappa)} \tag{55}$$

where the parameters have been arranged in a vector, $\boldsymbol{\Lambda}$.

The elements of $\mathbf{C}$ are complicated functions of the overlap and density matrices, and the elements of $\mathbf{Y}$ functions of the mean-fields and Hamiltonian matrix elements.

$$Y_{i\alpha} = \sum_l \rho_{il}\left(H_{il}^{(\alpha 0)} - \left[\mathbf{S}^{(\alpha 0)}\mathbf{S}^{-1}\mathbf{H}\right]_{il}\right) \tag{56}$$

$$C_{i\alpha,j\beta} = \rho_{ij}\left(S_{ij}^{(\alpha\beta)} - \left[\mathbf{S}^{(\alpha 0)}\mathbf{S}^{-1}\mathbf{S}^{(0\beta)}\right]_{ij}\right) \tag{57}$$

where α refers to a parameter and i to a function. The superscripted overlap and Hamiltonian matrices have elements involving the derivatives of the GWPs with respect to the parameters

$$S_{il}^{(\alpha\beta)} = \left\langle \frac{\partial g_i}{\partial \lambda_{i\alpha}} \middle| \frac{\partial g_l}{\partial \lambda_{l\beta}} \right\rangle \tag{58}$$

$$H_{il}^{(\alpha\beta)} = \left\langle \frac{\partial g_i}{\partial \lambda_{i\alpha}} \middle| \hat{H} \middle| \frac{\partial g_l}{\partial \lambda_{l\beta}} \right\rangle \tag{59}$$

which are simply Gaussian moments. For example, if $\lambda_{i\alpha} = \xi_i^{(\kappa)}$

$$S_{il}^{(\alpha 0)} = \left\langle \frac{\partial g_i}{\partial \xi_i^{(\kappa)}} \middle| g_l \right\rangle \quad = \langle g_i | Q_{(\kappa)} | g_l \rangle. \tag{60}$$

Note that, as for the usual SPFs, the projector out of the space spanned by GWP functions

$$1 - P = 1 - \sum_{ij} | \, g_i \rangle S_{ij}^{-1} \langle g_j \, | \tag{61}$$

is contained in both the **Y** vector and **C** matrix. This is one of the most important properties of the MCTDH method, ensuring that changes are made to the basis set only as dictated by the evolving wavepacket, and ensuring fast convergence.

The method is an exact quantum dynamics method provided all the integrals in the equations of motion are calculated exactly. In practice, the Hamiltonian matrix elements are evaluated by making use of a *local harmonic approximation* (LHA) in which the potential is expanded to second-order for each GWP

$$V_j = V_0 + \sum_{\alpha=1}^{f} V'_\alpha Q_\alpha + \frac{1}{2} \sum_{\alpha=1}^{f} V''_{\alpha\beta} Q_\alpha Q_\beta \tag{62}$$

where the value V_0 and the derivatives V'_α, $V''_{\alpha\beta}$ are evaluated at the centre point.

G-MCTDH can provide a useful link to other types of Gaussian wavepacket methods and time-dependent coherent-state basis set approaches. Following the work of Heller [84], most of these methods are based on GWPs that propagate along classical trajectories to model the true evolving wavefunction. These methods are all based on the well-known result from quantum mechanics that a wavefunction with a Gaussian shape in a harmonic potential retains its shape and the centre of the wavepacket follows the classical trajectory.

One can, for example, use a superposition of Gaussian functions with fixed widths, known as frozen Gaussians [85],

$$\Psi(\mathbf{x}, t) = \sum_i g_i(\mathbf{x}, t). \tag{63}$$

Writing the GWPs as separable products of one-dimensional functions with the form

$$g_j(x) = \exp \frac{1}{\hbar} (-a_j (x - x_j)^2 + i p_j (x - x_j) + i \gamma_j) \tag{64}$$

where a_j is the width, γ_j the phase, and the parameters x_j, p_j are the position and momentum of the centre of the function which evolve according to

$$\dot{x}_j = \frac{p_j}{m}$$
$$\dot{p}_j = -\frac{\partial V}{\partial x_j},$$

the classical equations of motion. Due to this underlying classical nature, these methods are not readily applicable to the description of quantum phenomena such as tunnelling and curve crossing. More sophisticated methods have been developed [86,87] and even applied to non-adiabatic systems [88]. These methods, however, suffer in general from numerical instabilities, insufficient coverage of the relevant phase space, and the fact that different initial choices for the representation of the wavefunction can lead to different results.

The spawning method of Martínez and co-workers [89,90] is aimed at describing non-adiabatic dynamics. It uses the ansatz

$$\Psi(\mathbf{x}, t) = \sum_j A_j g_j(\mathbf{x}, t). \tag{65}$$

The expansion coefficients introduce the coupling required to describe quantum phenomena, and have the same time-evolution as the G-MCTDH method, Equation (54), but the GWP basis functions follow classical trajectories. A clever algorithm is then used to 'spawn' new functions where they are required, e.g. when the wavepacket bifurcates in a region with strong non-adiabatic coupling. The method has been applied to a number of problems and successfully explains many observed phenomena in the photo-chemistry of polyatomic molecules.

Connection from classical-trajectory based Gaussian wavepacket methods to G-MCTDH can be made by first noting that the Gaussian functions in Equation (50) and Equation (64) are related by the transformation

$$\xi_\alpha = 2aq_\alpha + ip_\alpha. \tag{66}$$

Equations of motion for the centre of the G-MCTDH GWPs can be cast in a form that demonstrates the relationship to semi-classical methods [91]. In general,

$$\dot{q}_{l\beta} = \frac{p_{l\beta}}{m_\beta} + \dot{q}_{l\beta}^{\mathrm{corr}} \tag{67}$$

$$\dot{p}_{l\beta} = -V'_{l\beta} - \frac{4\zeta_{j\alpha}^2}{m_\alpha} q_{j\beta} + \sum_{\beta \neq \alpha} V''_{j\alpha\beta} q_{l\alpha} + \dot{p}_{l\beta}^{\mathrm{corr}}. \tag{68}$$

where $\dot{q}_{l\beta}^{\mathrm{corr}}$ and $\dot{p}_{l\beta}^{\mathrm{corr}}$ are terms containing correlations between the GWPs. If the Gaussians are uncoupled, for example if the basis set is complete, then these terms can be ignored. Furthermore, for coherent states in a harmonic potential,

$$\zeta_{j\alpha} = \frac{m_\alpha \omega_\alpha}{2}; \quad V''_\alpha = m_\alpha \omega_\alpha^2, \tag{69}$$

and the final two terms of Equation (68) cancel. Thus in this limit the GWPs in the G-MCTDH method follow classical trajectories.

This ideal coherent-state limit generally does not correspond to dynamical situations of interest and the coupling between GWPs means that they do not follow classical trajectories. The resulting convergence properties of the coupled trajectories are much better than classical trajectory based methods. There is also no dependence in the result on the choice of initial functions – the underlying variational character leads to the same result for the same number of functions however chosen initially. The coupling between the GWPs means that the method is also able to treat phenomena such as tunnelling and non-adiabatic transitions. In one of the first applications of the vMCG method to the

Henon–Heiles potential, tunnelling was observed, with GWPs escaping from the unbound potential [83].

The G-MCTDH method, like all the GWP methods, suffers from inherent numerical instabilities. The GWP phase factors cause fast oscillations in the overlap matrices, which are difficult to integrate, and the coupling between the expansion coefficients and GWP equations of motion is strong. And while the result may not depend on the choice of initial functions the numerics do. The solution is to use the relationship between the GWPs and an orthonormal set of functions that span the same space. This allows the coefficients to be propagated in the orthonormal basis (which approximates the MCTDH SPFs) while calculating all the matrix elements in the GWP basis. The resulting algorithm allows use of the efficient CMF integration scheme, and stable propagation with good step sizes results [91].

The first application to non-adiabatic dynamics was a study on the butatriene cation. The dynamics of this system calculated by different methods is shown in Figure 8. In (a) a comparison is made between wavepacket dynamics and trajectory surface

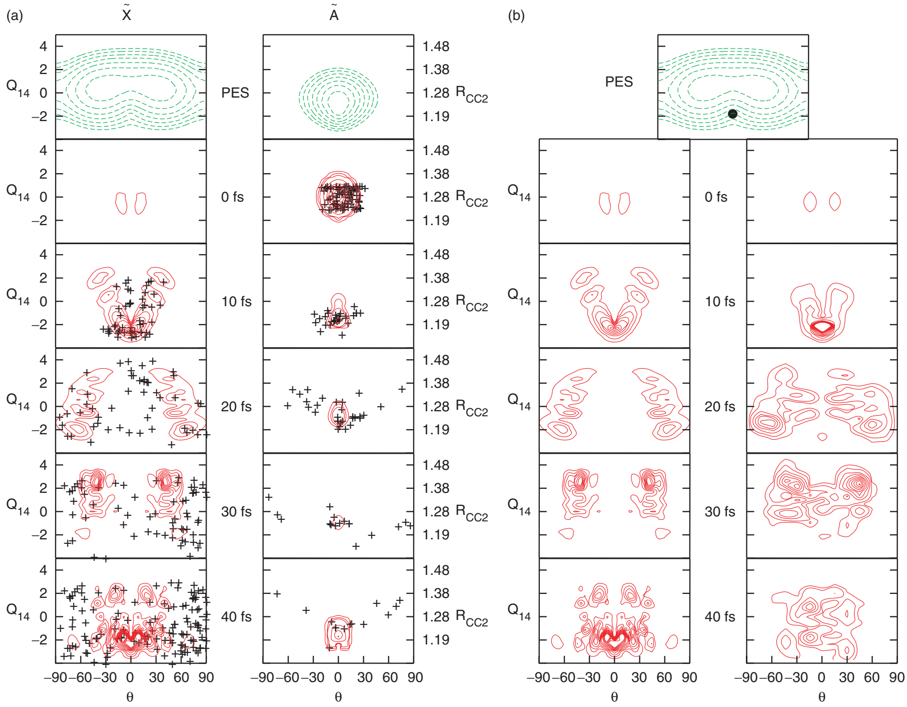

Figure 8. [Colour online] The wavepacket dynamics of the butatriene cation after formation in the diabatic $\tilde{A}$ state. (a) In the top panel, the contours show the adiabatic PESs of the $\tilde{X}$ and $\tilde{\mathrm{A}}$ states in the space of the main tuning and coupling modes. Lower panels show snapshots of the wavepacket at the times indicated. The contours are for the full quantum wavepacket the crosses denote the coordinates from 80 trajectories in a direct dynamics surface hopping study. Taken from Ref. [92]. (b) The wavepacket dynamics on the lower surface. On the left, the density is from a converged MCTDH calculation. On the right, from a vMCG calculation using 32 GWPs (16 in each state). Taken from [98].

hopping [92]. Surface hopping uses a 'swarm' of classical trajectories to simulate the evolving wavepacket. On reaching a region where non-adiabatic coupling is strong a trajectory may change from one surface to another according to a probability criterion. This is a simple form of molecular dynamics, easy to implement, applicable to large systems, and often able to deliver useful information. Surface hopping was introduced by Tully [93,96] and has been developed widely by Truhlar and co-workers (see [95,96] and references therein).

The five lower panels represent the evolving adiabatic wavepacket as snapshots of the density at 10 fs intervals. Eighty trajectories were run, and the coordinates of each are represented by crosses. These calculations were made using direct dynamics, with the PESs calculated on-the-fly using quantum chemistry calculations at the CASSCF level (for a review of direct dynamics see [28,97]). The contours are the adiabatic density taken from converged MCTDH calculations, using a vibronic coupling model Hamiltonian fit to the same level of electronic structure theory. The top panel shows the analytic potential energy surfaces as contours plotted in the space of the two modes that provide the main non-adiabatic coupling, the central C–C stretch vibration and the torsional motion. The tight upper cone is on the right-hand side, while on the left the lower surface shows the double minima and ridge caused by the coupling to the upper state. The wavepacket snapshots are plotted projected into the same space.

The dynamics start by a vertical excitation to the upper diabatic state. This is shown by the Gaussian shaped wavepacket on the upper adiabatic surface. A very small portion is also seen on the lower surface. The wavepacket moves across the upper cone and, after 10 fs, meets the conical intersection. At this point a large population crosses to the lower state, where it bifurcates and moves down the two channels on the lower adiabatic surface. After a further 30 fs the wavepacket returns to the intersection region and a recurrence occurs with population returning to the upper state.

The surface hopping calculations follow the initial dynamics well, with the trajectories clustering around the wavepacket. Density then appears on the lower surface at 10 fs and so the time-period for reaching the non-adiabatic region is correctly described. After this crossing, however, the trajectories no longer stay with the density and spread out over the surfaces. This is due to the lack of nuclear coherence in the surface hopping method.

Figure 8(b) compares the full wavepacket on the lower surface with that calculated by the vMCG method using a small basis set of only 32 GWPs [98], 16 in each state. The approximate wavepacket on the right panel is thus created using fewer trajectories than the surface hopping calculations. It is seen to follow the full packet qualitatively, including the bifurcation, the recurrence and some of the structure.

A more recent study benchmarks the G-MCTDH method, returning to the classic model of pyrazine examined above [91]. A comparison of the vMCG method to the use of classical GWPs was made to demonstrate the convergence properties. As the model is a second-order polynomial the converged result is identical to the full MCTDH one. Figure 9 shows the autocorrelation function for the four-mode pyrazine model in the two cases. The vMCG method already has the first peak correct with a mere 40 basis functions (20 in each state), and is converged with 160. In contrast the classical GWPs require a few hundred basis functions to get the first few peaks reasonable, and the autocorrelation is still not converged with many thousand functions.

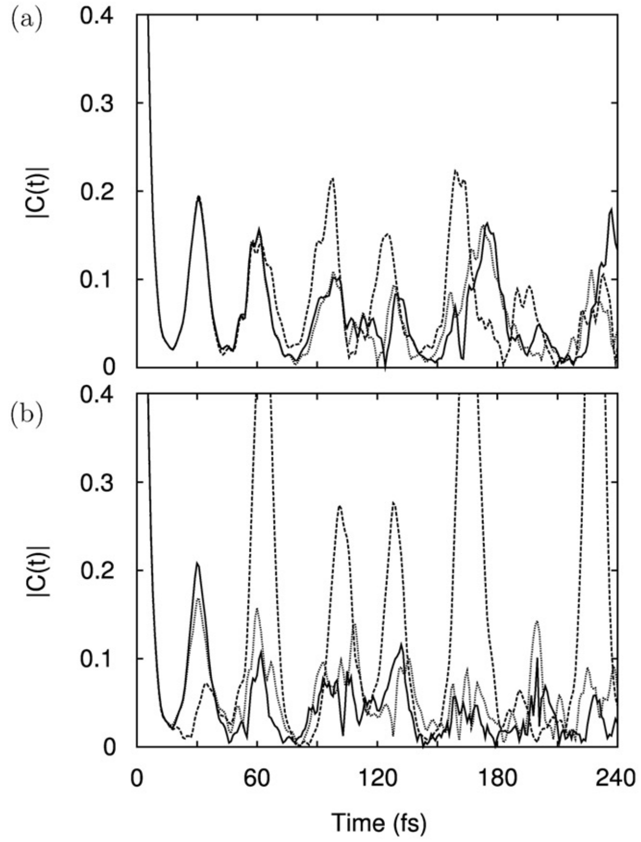

Figure 9. The autocorrelation function from a four-mode model of the S_1/S_2 manifold of pyrazine after vertical excitation to the S_2 state comparing vMCG to classical GWPs. (a) vMCG 40 (dashed), 120 (dotted) and 160 GWPs (bold line) (b) classical GWPs 160 (dotted), 3794 (dashed) and 94,320 (bold line) GWPs. Reproduced from [91].

A demonstration of the potential of the method is given in a 10-mode pyrazine model study. This takes the usual four-mode model and adds a further six-modes selected so that the autocorrelation function has a strong similarity to that from the full 24-mode calculation. The resources required are listed in Table 3 for calculations producing a converged 300 fs autocorrelation function using MCTDH, G-MCTDH and vMCG. Frozen Gaussians were used throughout.

The 10-modes were combined together into four-particles. In the MCTDH calculation, a primitive basis set of harmonic oscillator DVR functions was used for each mode. The numbers of these functions for each particle are listed in the first column. The single-particle functions were then described on a grid that is a product of the one-dimensional primitive grids. Thus, for example, the first particle had a primitive grid of $40 \times 32 = 1280$ points.

The G-MCTDH calculation treated the four-mode system using a primitive grid and the remaining modes using GWPs. The vMCG calculation treated all particles using GWPs. The number of SPFs or GWPs used for each particle are then listed, with a number

Table 3. Computer resources used for calculations of the absorption spectrum of the pyrazine molecule using a 10-mode model. The upper part of the table details the single-particle function and primitive basis. Column 1 lists the modes and how they were combined into particles. Column 2 gives the no. of harmonic oscillator DVR functions used for each mode. Columns 3–5 give the no. of single-particle functions used for each particle and each state using different methods. The lower part of the table details the resources required for each calculation. The first row shows how many numbers are required to describe the single-particle functions and GWPs. The second row how many numbers are required to describe the A-vector. The third and fourth rows show the memory and cpu-time required.

Modes	N	n (MCTDH)	n (G-MCTDH)	n (vMCG)
ν_{10a}, ν_{6a}	$(40, 32)$	14, 11	14, 11	60, 60
ν_1, ν_{8a}	$(20, 12)$	8, 7	8, 7	60, 60
$\nu_2, \nu_{6b}, \nu_{8a}, \nu_{8b}$	$(4, 8, 8, 24)$	10, 10	20, 20	20, 20
ν_{19b}, ν_{18b}	$(72, 80)$	10, 10	20, 20	20, 20
Num (SPFs)		273, 680	35, 900	1040
Num (A-vec)		18, 900	91, 600	2, 880, 000
Memory (MB)		148	49	406
CPU (hours)		11	3	58

for each state. Thus the MCTDH calculation required 14 SPFs for the ν_{10a}, ν_{6a} particle in the lower, S_1, state and 11 SPFs for the upper, S_2 state, while the vMCG calculation required 60 GWPs for this particle in both states.

The line Num (SPFs) shows how many numbers were required to represent the SPFs and GWPs. For the MCTDH calculation this is the number of grid points per function multiplied by the number of functions. For the GWPs each function requires one number per mode plus one $(\xi_j^{(\alpha)}, \eta_j)$. The effect of the fewer numbers required to represent the parametrized GWP functions is clear. The line Num (A-vec) is the number of expansion coefficients in the A-vector. Here it is clear the effect of the larger number of GWPs required compared to the SPFs. This is particularly the case for vMCG, where a lot of GWPs are needed to describe the wavepacket in the space of the strongly coupled modes.

The final effect of the payoff for fewer numbers to describe the basis functions using GWPs against the resultant more configurations is seen by the memory and CPU usage which are both smallest for the G-MCTDH calculation. Only 49 MB of memory and 3 hours of CPU-time is not much for a 10-mode quantum dynamics calculation of an autocorrelation function out to 300 fs. It should be noted here that a reasonable spectrum can be obtained using G-MCTDH with an SPF/GWP basis of [12,9], [6,5], [8,8], [10,10] functions for the particles in the order listed in the table. This required only 24 MB and 0.75 hrs and is shown in Figure 10. The peaks are all in the correct places, and the intensities are not far off. Thus the essential physics of the problem is being well described in a very cheap calculation.

9. Summary and conclusions

Conical intersections are now known to be ubiquitous in photo-chemistry, and an understanding of their properties is essential, yet difficult due to fact the nuclear and

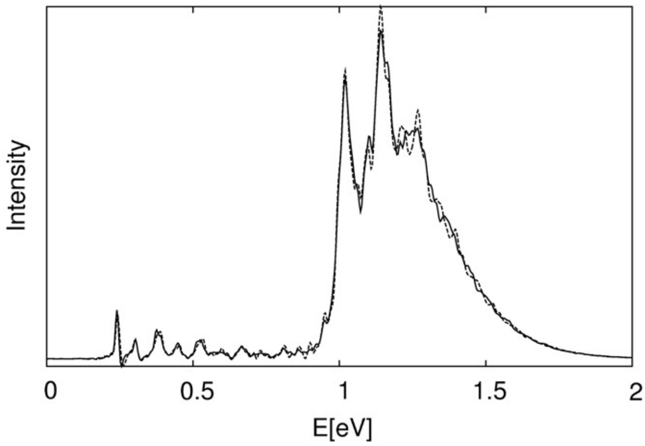

Figure 10. The spectrum from a 10-mode model of pyrazine using a converged MCTDH calculation (bold line) and a small G-MCTDH calculation (dashed line). See text for details.

electronic motion is coupled in this region. The nuclear dynamics must therefore be described using quantum mechanics, and the number of modes often coupled together in these systems is beyond the reach of most quantum dynamics methods.

The MCTDH method is a powerful tool, able to handle more nuclear degrees of freedom than standard wavepacket dynamics. The properties of the method, and how this is useful for multi-dimensional dynamics has been outlined above. In particular, the MCTDH equations conserve the norm and, for time-independent Hamiltonians, the total energy. MCTDH simplifies to Time-Dependent Hartree when only one basis function is used for each mode. Increasing the basis size recovers more and more correlation, until finally the standard method (i.e. propagating the wavepacket on the primitive basis) is used. Hence with MCTDH one can almost continuously switch from a cheap but less accurate calculation to a highly accurate but expensive one. This is a useful characteristic in the study of multi-dimensional systems.

The vibronic coupling model Hamiltonian provides a good starting point for the realistic study of photo-chemical systems in which non-adiabatic effects play an important role. It is also in the right form for MCTDH. In its simplest form, the linear vibronic coupling model, it has been shown to correctly describe the dynamics of a system as it passes close to and through a conical intersection connecting different electronic states. Extensions to higher orders then add more details, important for describing the dynamics at longer time-scales and at geometries away from the intersection. In this context recent work by Viel and Eisfeld should be mentioned. They have studied the importance of high order (up to the sixth power) terms on Jahn–Teller [99] and pseudo-Jahn–Teller systems [100] and applied the theory to the photodissociation of the ammonia cation [101].

Fitting the model to the adiabatic surfaces provided by electronic structure calculations provides a suitable way of providing the diabatic surfaces and couplings required without the necessity of defining the diabatic functions themselves. In fact the model provides a good way of providing these functions. The use of fitting routines can provide the many required parameters in a semi-automatic way from a small number of single-point *ab initio* calculations at suitable points.

Non-adiabatic dynamics is by its nature multi-dimensional: often the motion of a number of modes is coupled. Here the power of the MCTDH method has proved very successful in studying these systems. The form of the vibronic coupling model is automatically in the form required, and calculations including 10 or more modes and a number of electronic states are presently feasible. The systems studied to date have provided an invaluable insight into the dynamics of these systems.

On-going work will enable more modes to be treated with greater accuracy. The G-MCTDH is a step in this direction. A different approach, not covered in this review, is the multi-layer formalism implemented by Wang [102]. At the lowest level, the wavepacket is made up of an MCTDH wavefunction high-dimensional SPFs. These are then propagated using the MCTDH algorithm itself in a next layer using lower dimensional SPFs, and so on. In this way a spin-boson problem including thousands of modes can be treated [102]. This approach could tackle systems of hundreds of atoms, and be the way forward in using quantum dynamics to treat general chemical problems. Recent studies on proton transfer in condensed phases [103] and the electron transfer dynamics in the dye molecule coumarin bound to a semiconductor surface [21] highlight this potential.

A final development to be mentioned is the *effective mode* formalism [104–106]. This formalism will certainly help by providing a framework for the reduction of a huge system. After dividing the modes into a ‘system’ and a ‘bath’, the vibronic coupling model can be reformulated in a hierarchy of Hamiltonians, enabling an analysis of the important dynamics with a limited effort. This has been used, for example, to study the quantum dynamics in semi-conducting polymers [107].

The study of non-adiabatic systems is becoming a cornerstone of our understanding of photo-induced processes. Non-adiabatic systems are, however, naturally multi-dimensional quantum mechanical problems and thus hard to treat rigorously. In this review we have demonstrated how a combination of the vibronic coupling model Hamiltonian and the MCTDH wavepacket propagation algorithm can provide detailed information on real chemical physics problems. Future developments of the MCTDH method were also outlined that, together with extending the model to higher orders, will continue to enhance the ability to treat truly polyatomic – and even condensed phase – systems in greater detail with the requisite accuracy.

Acknowledgements

Parts of Sections 2–7 of this review are reproduced with permission of the publisher from the forthcoming book *High Dimensional Quantum Dynamics: Basic Theory, Extensions, and Applications of the MCTDH Method* [5].

References

[1] H. D. Meyer, U. Manthe, and L. S. Cederbaum, Chem. Phys. Lett. **165**, 73 (1990).
[2] U. Manthe, H. D. Meyer, and L. S. Cederbaum, J. Chem. Phys. **97**, 3199 (1992).
[3] M. H. Beck, A. Jäckle, G. A. Worth, *et al.*, Phys. Rep. **324**, 1 (2000).
[4] H. D. Meyer and G. A. Worth, Theor. Chem. Acc. **109**, 251, feature article (2003).

[5] H. D. Meyer, F. Gatti, and G. A. Worth, editors, *High Dimensional Quantum Dynamics: Basic Theory, Extensions, and Applications of the MCTDH Method* (VCH, Weinheim, Germany, 2008), In preparation.
[6] W. Domcke, D. R. Yarkony, and H. Köppel, editors, *Conical Intersections: Electronic Structure, Dynamics and Spectroscopy* (World Scientific, Singapore, 2004).
[7] G. A. Worth and L. S. Cederbaum, Ann. Rev. Phys. Chem. **55**, 127 (2004).
[8] U. Manthe and A. D. Hammerich, Chem. Phys. Lett. **211**, 7 (1993).
[9] A. D. Hammerich, U. Manthe, R. Kosloff, *et al.*, J. Chem. Phys. **101**, 5623 (1994).
[10] L. S. Cederbaum, W. Domcke, H. Köppel, *et al.*, Chem. Phys. **26**, 169 (1977).
[11] W. Domcke, H. Köppel, and L. S. Cederbaum, Mol. Phys. **43**, 851 (1981).
[12] H. Köppel, W. Domcke, and L. S. Cederbaum, Adv. Chem. Phys. **57**, 59 (1984).
[13] M. Klessinger, Angew. Chem. **107**, 597 (1995).
[14] M. A. Robb, F. Bernardi, and M. Olivucci, Pure and Appl. Chem. **67**, 783 (1995).
[15] S. Mahapatra and H. Köppel, J. Chem. Phys. **109**, 1721 (1998).
[16] H. Köppel, M. Döscher, and S. Mahapatra, Int. J. Quant. Chem. **80**, 942 (2000).
[17] M. Garavelli, P. Celani, F. Bernardi, *et al.*, J. Am. Chem. Soc. **119**, 6891 (1997).
[18] S. Hahn and G. Stock, J. Phys. Chem. B **104**, 1146 (2000).
[19] A. L. Sobolewski, W. Domcke, C. Dedonder-Lardeux, *et al.*, PCCP **4**, 1093 (2002).
[20] A. L. Sobolewski, W. Domcke, and C. Hättig, Proc. Nat. Acad. Sci. **102**, 17903 (2005).
[21] I. Kondov, M. Thoss, and H. Wang, J. Phys. Chem. C **111**, 11970 (2007).
[22] H. Wang, J. Chem. Phys. **113**, 9948 (2000).
[23] A. Raab, G. Worth, H.-D. Meyer, *et al.*, J. Chem. Phys. **110**, 936 (1999).
[24] H. Naundorf, G. Worth, H.-D. Meyer, *et al.*, J. Phys. Chem. **106**, 719 (2002).
[25] L. Wang, H. D. Meyer, and V. May, J. Chem. Phys. **125**, 014102 (2006).
[26] G. A. Worth, R. E. Carley, and H. H. Fielding, Chem. Phys. **338**, 220 (2007).
[27] I. Burghardt, H.-D. Meyer, and L. S. Cederbaum, J. Chem. Phys. **111**, 2927 (1999).
[28] G. A. Worth, M. A. Robb, and B. Lasorne, Mol. Phys. In press (2008).
[29] R. Kosloff, J. Phys. Chem. **92**, 2087 (1988).
[30] K. C. Kulander, ed, *Time-Dependent Methods for Quantum Dynamics* (Amsterdam, Elsevier, 1991).
[31] R. Kosloff, Ann. Rev. Phys. Chem. **45**, 145 (1994).
[32] U. Manthe, J. Chem. Phys. **105**, 6989 (1996).
[33] F. Huarte-Larrañaga and U. Manthe, J. Chem. Phys. **116**, 2863 (2002).
[34] F. Huarte-Larrañaga and U. Manthe, J. Chem. Phys. **117**, 4635 (2002).
[35] M. H. Beck and H. D. Meyer, Z. Phys. D **42**, 113 (1997).
[36] J. Y. Fang and H. Guo, J. Chem. Phys. **101**, 5831 (1994).
[37] G. A. Worth, H. D. Meyer, and L. S. Cederbaum, J. Chem. Phys. **105**, 4412 (1996).
[38] R. Schinke, *Photodissociation Dynamics* (Cambridge University Press, Cambridge, 1993).
[39] G. G. Balint-Kurti, R. N. Dixon, and C. C. Marston, J. Chem. Soc., Faraday Trans. **86**, 1741 (1990).
[40] U. Manthe, H. D. Meyer, and L. S. Cederbaum, J. Chem. Phys. **97**, 9062 (1992).
[41] V. Engel, Chem. Phys. Lett. **189**, 76 (1992).
[42] S. Mahapatra, G. A. Worth, H.-D. Meyer, *et al.*, J. Phys. Ghem. **A 105**, 5567 (2001).
[43] A. Jäckle and H. D. Meyer, J. Chem. Phys. **104**, 7974 (1996).
[44] A. Jäckle and H. D. Meyer, J. Chem. Phys. **109**, 3772 (1998).
[45] M. R. Brill, F. Gatti, D. Lauvergnat, *et al.*, Chem. Phys. **338**, 186 (2007).
[46] G. A. Worth, H. D. Meyer, and L. S. Cederbaum, J. Chem. Phys. **109**, 3518 (1998).
[47] M. Baer, Chem. Phys. Lett. **35**, 112 (1975).
[48] V. Sidis, Adv. Chem. Phys. **82**, 73 (1992).
[49] T. Pacher, L. S. Cederbaum, and H. Köppel, Adv. Chem. Phys. **84**, 293 (1993).
[50] C. A. Mead and D. G. Truhlar, J. Chem. Phys. **77**, 6090 (1982).

[51] R. Englman, *The Jahn–Teller Effect in Molecules and Crystals* (John Wiley, New York, 1972).
[52] I. B. Bersuker and V. Z. Polinger, *Vibronic Interactions in Molecules and Crystals* (Springer Verlag, Heidelberg, 1989).
[53] M. Döscher, H. Köppel, and P. G. Szalay, J. Chem. Phys. **117**, 2645 (2002).
[54] H. Köppel, J. Gronki, and S. Mahapatra, J. Chem. Phys. **115**, 2377 (2001).
[55] H. Köppel and B. Schubert, Mol. Phys. **104**, 1069 (2006).
[56] H. Köppel, B. Schubert, and H. Lischka, Chem. Phys. **343**, 319 (2008).
[57] I. Yamazaki, T. Murao, T. Yamanaka, *et al.*, Faraday Discuss. Chem. Soc. **75**, 395 (1983).
[58] L. Seidner, G. Stock, A. L. Sobolewslri, *et al.*, J. Chem. Phys. **96**, 5298 (1992).
[59] S. Krempl, M. Winterstetter, H. Plöhn, *et al.*, J. Chem. Phys. **100**, 926 (1994).
[60] F. Brogli, E. Heilbronner, E. Kloster-Jensen, *et al.*, Chem. Phys. **4**, 107 (1974).
[61] P. Baltzer, B. Wannberg, M. Lundqvist, *et al.*, Chem. Phys. **196**, 551 (1995).
[62] C. Woywod and W. Domcke, Chem. Phys. **162**, 349 (1992).
[63] L. S. Cederbaum, W. Domcke, and H. Köppel, Chem. Phys. **33**, 319 (1978).
[64] S. Mahapatra, L. S. Cederbaum, and H. Köppel, J. Chem. Phys. **111**, 10452 (1999).
[65] G. Worth and L. Cederbaum, Chem. Phys. Lett. **348**, 477 (2001).
[66] C. Cattarius, A. Markmann, and G. A. Worth, The VCHAM Program. (2003) See http://www.pci.uni-heidelberg.de/tc/usr/mctdh/
[67] G. A. Worth, M. H. Beck, A. Jäckle, *et al.*, *The MCTDH Package*, Version 8.3, See http://mctdh.uni-hd.de/
[68] C. Cattarius, G. A. Worth, H.-D. Meyer, *et al.*, J. Chem. Phys. **115**, 2088 (2001).
[69] G. A. Worth, J. Photochem. Photobiol. **A 190**, 190 (2007).
[70] A. Markmann, G. A. Worth, and L. S. Cederbaum, J. Chem. Phys. **122**, 144320 (2005).
[71] A. Markmann, G. A. Worth, S. Mahapatra, *et al.*, J. Chem. Phys. **123**, 204310 (2005).
[72] M. J. Paterson, P. A. Hunt, M. A. Robb, *et al.*, J. Phys. Chem. **A 106**, 10494 (2002).
[73] G. A. Worth, G. Welch, and M. J. Paterson, Mol. Phys. **104**, 1095 (2006).
[74] J. Schön and H. Köppel, J. Chem. Phys. **103**, 9292 (1995).
[75] S. A. Trushin, W. Fuß, and W. E. Schmid, Chem. Phys. **259**, 313 (2000).
[76] H. Köppel, M. Döscher, I. Baldea, *et al.*, J. Chem. Phys. **117**, 2657 (2002).
[77] P. Baltzer, L. Karlsson, B. Wannberg, *et al.*, Chem. Phys. **224**, 95 (1997).
[78] I. Baldea and H. Köppel, J. Chem. Phys. **124**, 064101 (2006).
[79] I. Baldea, J. Franz, P. G. Szalay, *et al.*, Chem. Phys. **329**, 65 (2006).
[80] E. Gindensperger, I. Baldea, J. Franz, *et al.*, Chem. Phys. **338**, 207 (2007).
[81] S. Faraji, H.-D. Meyer, and H. Köppel, J. Chem. Phys. In press (2008).
[82] I. Burghardt, M. Nest, and G. A. Worth, J. Chem. Phys. **119**, 5364 (2003).
[83] G. Worth and I. Burghardt, Chem. Phys. Lett. **368**, 502 (2003).
[84] E. J. Heller, J. Chem. Phys. **62**, 1544 (1975).
[85] E. J. Heller, J. Chem. Phys. **75**, 2923 (1981).
[86] S. Sawada, R. Heather, B. Jackson, *et al.*, J. Chem. Phys. **83**, 3009 (1985).
[87] D. V. Shalashilin and M. S. Child, J. Chem. Phys. **115**, 5367 (2001).
[88] S. Sawada and H. Methiu, J. Chem. Phys. **84**, 227 (1986).
[89] T. J. Martínez, M. Ben-Nun, and R. D. Levine, J. Phys. Chem. **100**, 7884 (1996).
[90] M. Ben-Nun and T. J. Martínez, J. Chem. Phys. **108**, 7244 (1998).
[91] I. Burghardt, K. Giri, and G. A. Worth, J. Chem. Phys. Submitted (2008).
[92] G. Worth, P. Hunt, and M. Robb, J. Phys. Chem. A **107**, 621 (2003).
[93] J. C. Tully and R. K. Preston, J. Chem. Phys. **55**, 562 (1971).
[94] J. C. Tully, J. Chem. Phys. **93**, 1061 (1990).
[95] M. S. Topaler, M. D. Hack, T. C. Allison, *et al.*, J. Chem. Phys. **106**, 8699 (1997).
[96] M. D. Hack and D. G. Truhlar, J. Phys. Chem. A **104**, 7917 (2000).
[97] G. A. Worth and M. A. Robb, Adv. Chem. Phys. **124**, 355 (2002).
[98] G. A. Worth, M. A. Robb, and I. Burghardt, Farad. Discuss. **127**, 307 (2004).

[99] A. Viel and W. Eisfeld, J. Chem. Phys. **120**, 4603 (2004).
[100] W. Eisfeld and A. Viel, J. Chem. Phys. **122**, 204317 (2005).
[101] A. Viel, W. Eisfeld, S. Neumann, *et al.*, J. Chem. Phys. **124**, 214306 (2006).
[102] H. Wang and M. Thoss, J. Chem. Phys. **119**, 1289 (2003).
[103] I. R. Craig, H. Wang, and M. Thoss, J. Chem. Phys. **127**, 144503 (2007).
[104] E. Gindensperger, I. Burghardt, and L. S. Cederbaum, J. Chem. Phys. **124**, 144103 (2006).
[105] E. Gindensperger, I. Burghardt, and L. S. Cederbaum, J. Chem. Phys. **124**, 144104 (2006).
[106] L. S. Cederbaum, E. Gindensperger, and I. Burghardt, Phys. Rev. Lett. **94**, 113003 (2005).
[107] H. Tamura, J. G. S. Ramon, E. R. Bittner, *et al.*, Phys. Rev. Lett. **100**, 107402 (2008).
[108] G. A. Worth, H. D. Meyer, and L. S. Cederbaum, Chem. Phys. Lett. **299**, 451 (1999).
[109] S. Saddique and G. A. Worth, Chem. Phys. **329**, 99 (2006).
[110] T. J. Penfold and G. A. Worth, J. Mol. Graph. Mod. **26**, 613 (2007).
[111] E. V. Gromov, A. B. Trofimov, N. M. Vitkovskaya, *et al.*, J. Chem. Phys. **121**, 4585 (2004).
[112] T. S. Venkatesan, S. Mahapatra, H.-D. Meyer, *et al.*, J. Phys. Chem. **A 111**, 1746 (2007).